Female mice lacking GluA3 show early onset of hearing loss, synaptopathy, and afferent swellings in ambient sound levels

Indra Pal[1], Atri Bhattacharyya[2], Babak V-Ghaffari[2], Essence D. Williams[1], Maolei Xiao[2], Mark A. Rutherford[2], and María Eulalia Rubio[1,3]*

1. Department of Neurobiology, University of Pittsburgh School of Medicine, Pittsburgh, PA 15261

2. Department of Otolaryngology, Washington University School of Medicine, St. Louis, MO 63110

3. Department of Otolaryngology, University of Pittsburgh School of Medicine, Pittsburgh, PA 15261

Short title**:** Sex-dependent auditory phenotype in mice lacking *Gria3*

Keywords: confocal immunofluorescence; molecular anatomy; ultrastructure; AMPA receptors; hearing loss; inner hair cells; auditory nerve fibers; 3D reconstructions; ribbon synapses; *Gria3*

Number of text pages: 52

Number of Figures: 9

Number of Tables: 2

Number of words for Abstract: 175

Number of words for Introduction: 675

Number of words for Discussion: 2,589

*Corresponding Author

María Eulalia Rubio MD/PhD; e-mail: Mer@pitt.edu

Department of Neurobiology; University of Pittsburgh Medical School

BST3 Building, 3501 Fifth Avenue #10016, Pittsburgh, PA 15261

Abstract

AMPA-type glutamate receptors (AMPAR) mediate excitatory cochlear transmission. However, the unique roles of AMPAR subunits are unresolved. Lack of subunit GluA3 (*Gria3*^{KO}) in male mice reduced cochlear output by 8-weeks of age. Since *Gria3* is X-linked and considering sex differences in hearing vulnerability, we hypothesized accelerated presbycusis in *Gria3*^{KO} females. Here, auditory brainstem responses (ABR) were similar in 3-week-old female *Gria3*^{WT} and *Gria3*^{KO} mice. However, when raised in ambient sound, ABR thresholds were elevated and wave-1 amplitudes were diminished at 5-weeks and older in *Gria3*^{KO}. In contrast, these metrics were similar between genotypes when raised in quiet. Paired synapses were similar in number, but lone ribbons and ribbonless synapses were increased in female *Gria3*^{KO} mice in ambient sound compared to *Gria3*^{WT} or to either genotype raised in quiet. Synaptic GluA4:GluA2 ratios increased relative to *Gria3*^{WT}, particularly in ambient sound, suggesting an activity-dependent increase in calcium-permeable AMPARs in *Gria3*^{KO}. Swollen afferent terminals were observed by 5-weeks only in *Gria3*^{KO} females reared in ambient sound. We propose that lack of GluA3 induces sex-dependent vulnerability to AMPAR-mediated excitotoxicity.

Introduction

The α-amino-3-hydroxy-5-methyl-4-isoxazolepropionic acid receptors (AMPARs) are tetrameric glutamate-gated ion channels with pore-forming subunits GluA1-4 encoded by a family of genes, *Gria1-4*. Each subunit contributes to ionic permeability, pharmacological sensitivity, intracellular trafficking, synapse development, and activity-dependent plasticity of the channel. GluA1 and GluA2 are the most abundant subunits, relatively ubiquitous in the central nervous system, and prominently determining AMPAR plasticity and function, respectively (Shanks et al., 2012; Bassani et al., 2013; Purkey and Dell'Acqua, 2020). In particular, the absence of GluA2 from the AMPAR tetramer increases the unitary current and makes it permeable to Ca^{2+} in addition to Na^{+}

ions. In the adult hippocampus and cortex, the canonical Ca^{2+}-permeable AMPAR (CP-AMPAR) involved in synaptic plasticity is the GluA1 homomeric channel. GluA3 and GluA4 have more unique expression patterns, tending to be found at synapses with relatively fast kinetics, such as those in the cochlea and auditory brainstem (Wang et al., 1998; Rubio et al., 2017; Rutherford et al., 2023). Interestingly, the mature cochlea and auditory brainstem do not express GluA1, but they do express CP-AMPARs comprised of GluA3 and GluA4 subunits.

In male mice, the pore-forming subunit GluA3 of the AMPAR is essential for the development and maintenance of the cochlear afferent 'ribbon' synapses that underlie hearing function. Wild-type and $GluA3^{KO}$ mice raised in ambient sound levels had similar hearing sensitivities at one month of age, although ribbon synapses already exhibited ultrastructural and molecular alterations. These alterations include defective position-dependent maturation of pre- and post-synaptic specializations along an axis of structural and functional differentiation, as well as an imbalance of post-synaptic GluA subunit expression – an increase in GluA4 and decrease in GluA2 – suggesting a shift toward greater permeability to Ca^{2+} (Rutherford et al., 2023). At 2 months, the cochleae of male $GluA3^{KO}$ mice were less sensitive to suprathreshold sounds (lower wave-1 amplitude of the Auditory Brainstem Response, ABR), and by 3 months of age, they were less excitable by low-level sounds (elevated ABR threshold; García-Hernández et al., 2017). These results showed that synaptic anatomical defects preceded synapse dysfunction and hearing loss in male mice lacking GluA3, suggesting a synaptic vulnerability associated with AMPA receptor subunit imbalance in postnatal development that resulted in functional impairment of the mature cochlea.

A non-invasive functional assay of cochlear afferent transmission is wave-1 of the ABR, reflecting synchronous action potential generation in the auditory nerve at the onset of sound. With louder

sounds, ABR wave-1 becomes larger. As synapses are lost or the spikes they evoke become less synchronous, ABR wave-1 becomes smaller. In adult mice, females have larger wave-1 amplitudes than males (Lozier et al., 2023; Milon et al., 2018; Rouse et al., 2020). Also, female synapses appear to be more resistant to noise-induced hearing loss, and their wave-1 amplitudes are more resistant to reduction in size following noise exposure (Milon et al., 2018; Shuster et al., 2021); these sex differences seem related to estradiol. However, the effector molecules mediating these differences have yet to be discovered. Analysis of sex-dependent mRNA expression in the mouse cochlea suggests that *Gria2-4* levels were similar overall but that females had more neurons with higher *Gria3* mRNA relative to *Gria2* and a greater abundance of fast-gating *flop* isoforms (Lozier et al., 2023). Interestingly, in humans and rodents, *Gria3* is located on the X-chromosome (Gécz et al., 1999; Li and Carrel, 2008), where, at least in fibroblasts, the gene is subject to X-inactivation. Here, we studied adolescent and mature female GluA3^{KO} mice raised in an ambient or low-level sound vivarium. We find that female mice are more sensitive to the absence of GluA3 than male mice. Indeed, raising female mice in a vivarium with normal ambient levels of sound resulted in early cochlear synaptopathy and hearing loss, whereas this effect was prevented by rearing in a low-level sound vivarium. In ambient sound, like males, cochlear synapses in female *Gria3^{KO}* mice had less GluA2 and more GluA4 relative to *Gria3^{WT}*. Thus, cochlear synapses rely on GluA3 subunits for proper structure and function, and we conclude that females depend on GluA3 to a greater degree than males.

Results

Cochlear output is reduced in 5-week-old GluA3^{KO} female mice raised in ambient sound but unaltered when raised in quiet

To determine if GluA3 is indispensable for hearing in females, we raised female mice in the same ambient sound levels as males (**Fig. 1A**). Our data show that 5-week female GluA3^{KO} mice had

significantly elevated pure tone thresholds at 12, 16, and 32 kHz ($p < 0.05$, two-way ANOVA) (**Fig. 1B top left**). Although there was an insignificant trend toward elevated response thresholds for all stimuli tested, the wild-type and GluA3^{KO} mice had statistically similar thresholds in response to clicks as well as 4, 8, and 24 kHz tones ($p = 0.75$, two-way ANOVA). In contrast to the male GluA3^{KO} mice (Rutherford et al., 2023) and the female GluA3^{WT}, the female KO mice had significantly smaller clicks wave-1 amplitudes above 65 dB SPL ($p < 0.05$, two-way mixed ANOVA) (**Fig. 1B bottom left**). To determine if reduced cochlear sensitivity in female GluA3^{KO} persisted, we further tested the mice at 2 months (P60) and 3 months (P90) of age, with similar findings. At P60, ABRs (mean ± SD) show that mice raised in ambient sound levels have similar click thresholds between genotypes; however, the GluA3^{KO} have elevated pure tone thresholds at middle and high frequencies and reduced wave-1 amplitude as a function of sound intensity at P35, P60 and P90 (clicks $p = 0.75$, pure tones $p < 0.05$, two-way ANOVA; wave-1 amplitude $p < 0.05$, two-way mixed ANOVA) (**Fig. 1B top and bottom center**). Wave-1 latency was similar between GluA3^{KO} and GluA3^{WT} at all ages tested. Our findings show that the lack of AMPA receptor subunit GluA3 accelerates the hearing loss of females raised in ambient sound levels.

We then asked if the hearing sensitivity of female GluA3^{KO} mice was already affected before 5 weeks postnatal. Thus, we measured ABR in P20 female GluA3^{WT} and GluA3^{KO} mice raised in very low-level sound ("quiet," 10 dB SPL for mouse hearing; See Methods; **Fig. 1A**) compared to the normal vivarium ambient sound (40 dB SPL for mouse hearing). Data showed no difference between genotypes in ABR thresholds or wave-1 amplitudes at P20 (clicks $p > 0.05$, pure tones $p > 0.05$, two-way ANOVA; wave-1 amplitude $p > 0.05$, two-way mixed ANOVA), indicating relatively normal development of hearing function in GluA3^{KO} female mice when raised in quiet conditions. Next, we aged the GluA3^{WT} and GluA3^{KO} mice up to three months in the quiet and performed ABRs at P35, P60 and P90 (**Fig. 1C**). In contrast to mice raised in the normal vivarium,

there was no difference between genotypes in ABR click threshold, pure-tone threshold, or wave-1 amplitude at any age for mice raised in quiet (clicks $p > 0.05$, pure tones $p > 0.05$, two-way ANOVA; wave-1 amplitude $p > 0.05$ two-way mixed ANOVA) (**Fig. 1C top and bottom**). Wave-1 latency was also similar between the GluA3^{WT} and GluA3^{KO} mice.

We next analyzed wave-1 amplitude as a function of stimulus level (input/output (I/O) slope) between the two genotypes from P20 to P90 in ambient and in quiet (**Fig. 1D**). In ambient sound, we found that I/O slope at P35, P60, and P90 was significantly lower in GluA3^{KO} than GluA3^{WT} ($p < 0.05$, two-way ANOVA; **Fig. 1D left**). In contrast, we did not observe any difference in I/O slope between genotypes in quiet conditions ($p > 0.05$, two-way ANOVA; **Fig. 1D right**). As expected, I/O slope decreased with cochlear maturation and subsequent aging (Abdala and Dhar, 2012; Konrad-Martin et al., 2012; Johannesen and Lopez-Poveda, 2021). Interestingly, the largest reduction in I/O slope occurred for GluA3^{KO} mice raised in ambient sound between P20 to P35 (**Fig. 1D**), suggesting an activity-dependent requirement for GluA3 during maturation of the cochlea in the presence of ambient sound. This effect on wave-1 amplitude suggests poor synchrony of action potential generation in the auditory nerve, potentially caused by synaptopathy in GluA3^{KO} female mice raised in ambient conditions.

Ambient sound triggers hearing loss in female GluA3^{KO} mice

As described above, raising the mice in ambient sound levels from P20 to P90 elevated cochlear thresholds and reduced ABR wave-1 in the auditory nerve. Figure 2 compares ABR thresholds and wave-1 amplitudes for WT (**Fig. 2A**) or KO (**Fig. 2B**) in ambient vs. quiet conditions at P35, P60 and P90. In GluA3^{WT} female mice, we did not observe any differences in click thresholds, pure-tone thresholds, or wave-1 amplitudes in ambient or quiet sound at any age (clicks $p > 0.05$, pure tones $p > 0.05$, two-way ANOVA; wave-1 amplitude $p > 0.05$, two-way mixed ANOVA)

(**Tables 1 and 2**). In GluA3^{KO} mice, click and pure-tone thresholds were similar at all ages tested, like GluA3^{WT} (clicks $p > 0.05$, pure tones $p < 0.05$, two-way ANOVA). In contrast, wave-1 amplitude was significantly lower at all ages in GluA3^{KO} mice raised in ambient compared to those in quiet ($p < 0.05$ two-way mixed ANOVA) (**Fig. 2B**).

In mice, the first postnatal month is a sensitive and critical period for the development of inner hair cell (IHC) ribbon synapses and cochlear function (Rutherford and Moser, 2016; Wong et al., 2014; Michalski et al., 2019). After the postnatal onset of hearing function at the end of the 2nd postnatal week, cochlear function continues to develop with the maturation of afferent axonal and synaptic anatomies (Wong et al., 2013; 2014; Kim and Rutherford, 2016; Payne et al., 2021). Next, we asked if this reduction in wave-1 amplitude in female mice lacking GluA3 and raised in ambient sound was associated with cochlear synaptopathy: the pathological alteration, degradation, or loss of ribbon synapses.

Ambient sound triggers synaptopathy in female GluA3^{KO} mice

To assess cochlear synapses at 5 weeks of age with confocal microscopy, we immunolabelled the presynaptic ribbon and the postsynaptic AMPARs. Female GluA3^{WT} and GluA3^{KO} mice had similar numbers of paired synapses (juxtaposed pre- and post-synaptic markers) throughout the cochlea in both ambient and quiet conditions ($p > 0.05$, Two-tailed Mann-Whitney U test with Holm- Šidák's correction for multiple comparisons; **Fig. 3A left and right**). In contrast, the number of lone ribbons (anti-CtBP2 without juxtaposed postsynaptic markers) and the number of ribbonless synapses (anti-GluA2 and -GluA4 without juxtaposed CtBP2) was significantly greater throughout the cochlea in GluA3^{KO} compared to WT, but only in ambient sound ($p < 0.001$; Two-tailed Mann-Whitney U test with Holm- Šidák's correction for multiple comparisons; **Fig. 3B-C left**). In quiet conditions, GluA3^{KO} had significantly fewer ribbonless synapses in some cochlear

regions ($p < 0.05$) and overall ($p < 0.001$; **Fig. 3C right**), while lone ribbons in quiet were similar to WT ($p > 0.05$; **Fig. 3B right**). Relative to paired synapses (~ 15 per IHC), lone ribbons and ribbonless synapses were relatively rare in quiet and in WT in ambient sound (~ 0 – 2 per IHC, mean among images; group means of ~ 1 per IHC). However, in GluA3^{KO} raised in ambient sound the group means were > 2 per IHC (**Fig. 3B-C left**).

Some synapses (partially-paired) contained a presynaptic ribbon juxtaposed to only GluA2 or, very rarely, only GluA4. In ambient sound, GluA3^{KO} had significantly fewer GluA2-only synapses than WT ($p < 0.001$; Two-tailed Mann-Whitney U test with Holm- Šidák's correction for multiple comparisons; **Fig. 3D left**) and an insignificant trend toward a greater number of GluA4-only synapses than WT ($p > 0,05$; **Fig. 3E left**). In quiet, both varieties of partially-paired synapses were very rare: GluA2-only synapses were rarely seen in either genotype (**Fig. 3D right**), while GluA4-only synapses were seen only in GluA3^{KO} (**Fig. 3E right**). GluA4-only synapses were seen only in GluA3^{KO} for females in ambient or quiet conditions. Although GluA4-only synapses were significantly greater in number in GluA3^{KO} males than WT raised in ambient conditions (Rutherford et al., 2023), the differences did not reach statistical significance for the females ($p > 0,05$, All synapses ambient, **Fig. 3E left**; $p > 0,05$, All synapses quiet, **Fig. 3E right**).

Next, we compared synapse size and protein expression based on immunofluorescence volume and intensity per synapse, displayed as means per image and per group after normalizing metrics from individual images to the respective WT mean for images from ambient or quiet conditions (**Fig. 4**). Experiments were performed with GluA3^{KO} and GluA3^{WT} in parallel, separately for the two sound conditions, so comparisons are made only between GluA3^{WT} and GluA3^{KO}. The overall volume of paired synapses appeared significantly smaller in GluA3^{KO} in quiet compared to GluA3^{WT}; the two genotypes were similar in ambient sound. CtBP2 intensity did not differ by

genotype in either condition. For GluA4 and GluA2 intensity per synapse in quiet conditions, the variance between images was relatively small, and the decrease in GluA2 intensity in the GluA3^{KO} was significant ($p < 0.01$; **Fig. 4B**). For GluA4 and GluA2 intensity per synapse in ambient sound, we observed the same trends as in the males: an increase in GluA4 and a decrease in GluA2 in GluA3^{KO}. Although these two trends did not reach statistical significance in ambient sound due to increased variance ($p > 0.05$; **Fig. 4A-B**), the GluA4:GluA2 ratios were significantly increased in both quiet and ambient sound (100% increase in ambient vs. 60% increase in quiet ($p < 0.001$; **Fig. 4C**). We next asked if synapses without a ribbon differed in GluA4:GluA2 ratio from synapses with a ribbon by comparing the ratios between those two groups of synapses within each image. Only in GluA3^{WT} mice in ambient conditions, the GluA4:GluA2 ratios were significantly elevated at ribbonless synapses compared to paired synapses ($p < 0.05$; **Fig. 4D**).

At 5 weeks, the female GluA3^{KO} mice raised in quiet had apparently normal ABR (**Fig. 1-2**) and numbers of paired synapses (**Fig. 3**). Still, they had significantly reduced expression of GluA2 per synapse (**Fig. 4**). Next, we looked within synapses for additional anatomical synaptopathy. Similar to a previous study (Hu et al., 2020), we selected well-isolated synapses and divided each synapse into nanodomains to measure the GluA4:GluA2 fluorescence ratio (**Fig. 5A-B**; see Methods). In both genotypes, we observed a broad range of ratios within nanodomains, generally between ~ 0.1 – 2.0. However, in GluA3^{KO}, the ratios for whole synapses and nanodomains extended to greater values than in GluA3^{WT}, suggesting a greater fraction of AMPARs lacking the subunit GluA2 in GluA3^{KO} (**Fig. 5C-E**). For whole synapses in WT: mean ratio 0.58 ± 0.13, range 0.29 – 0.95; in KO: mean ratio 0.76 ± 0.23, range 0.31 – 1.42. For nanodomains in WT: mean ratio 0.53 ± 0.24, range 0.099 – 1.77; in KO: mean ratio 0.70, range 0.12 – 2.8. Indeed, the probability distributions for synapses and nanodomains differed between GluA3^{WT} and GluA3^{KO} (KS test: synapses, $p = 7.2\ e^{-9}$; nanodomains, $p = 3.5\ e^{-19}$). The positive relationship between

GluA4:GluA2 ratio and ribbon fluorescence per synapse is shown in **Figure 5F**, and the strength of the correlation was tested with Spearman's coefficient r_s. For GluA3^{WT}, the correlation was significant (r_s 0.26 > critical value 0.18); for GluA3^{KO}, the correlation was not significant (r_s 0.092 < critical value 0.18).

In the same set of synapses from female mice raised in quiet, we asked if the GluA4:GluA2 fluorescence ratios differed as a function of distance from the center of the synapse with radial distributions (**Fig. 6**; see Methods). Shells of pixel areas were created from concentric squares overlaid on maximum-intensity projections of Airyscan images in GluA3^{WT} and KO (**Fig. 6A-B**). For each fluorescence channel in each shell, the sum of pixel intensities was divided by the number of pixels to calculate shell density, and the GluA4:GluA2 density ratios were calculated for each shell in each synapse based on the raw values or the peak-normalized values (**Fig. 6C-D**). Radial distributions of GluA4:GluA2 fluorescence ratio per synapse were grouped by genotype in 6 tonotopic regions (**Fig. 6E-F**). This analysis confirmed the observation of greater GluA4:GluA2 fluorescence ratios in GluA3^{KO} relative to WT and shows this to be the case throughout intrasynaptic space when comparing similar tonotopic regions. On average, ratios tended to peak 200 – 400 nm from the synapse center in both genotypes, but this peak was less pronounced in GluA3^{KO} because GluA4:GluA2 ratios tended to be greater near the synapse center in GluA3^{KO} relative to GluA3^{WT}. Thus, it appears that lack of GluA3 alters the intrasynaptic distribution of GluA2 and GluA4.

Afferent swellings in the 5-week-old female GluA3^{KO} in ambient.

To look for structural correlates of hearing impairment in the GluA3-deficient cochlea, we analyzed ultrastructurally the sensory epithelium of the mice raised in ambient and quiet sound conditions. The general structure and cellular components of the sensory epithelium of the female GluA3^{KO}

raised in ambient and quiet were similar to GluA3^{WT} and published data of C57BL/6 mice (e.g., Ohlemiller and Gagnon, 2004). However, in the P35 female KO raised in ambient conditions, we noticed the existence of vacuoles underneath IHCs, which were most often observed in the high-frequency, basal part of the cochlear spiral (**Fig. 7D, F, G**). We confirmed that the vacuoles corresponded to swellings of Type I afferent terminals synapsing on both sides of the IHCs (modiolar and pillar, **Fig. 7F, G**). Relative to other parts of the neuronal cytoplasm, these vacuoles were clearer, suggesting less density of electron-absorbing intracellular material. Some afferent swellings had a post-synaptic density (PSD) juxtaposed with a membrane-anchored pre-synaptic ribbon (**Fig. 7F)**, whereas others were ribbonless (**Fig. 7G**). The cytoplasm of the swollen afferents showed missing mitochondria and swollen endoplasmic reticulum. Alongside the swollen afferents, normal-looking afferent terminals with electron-dense PSDs and membrane-anchored presynaptic ribbons were present (**Fig. 7E**). We calculated the average gray value (AGV) of the cytoplasm of the afferent terminals and found that in the GluA3^{KO} the cytoplasm of the swollen afferents (AGV mean = 150 $\pm$ 23.4 $\pm$SD; AGV scale settings black= 0 and white= 255) was significantly lighter than the “normal-looking” afferents in the KO (AGV mean = 105 $\pm$ 20.2 $\pm$SD) or the GluA3^{WT} afferents (AGV mean = 102 $\pm$ 11.6 $\pm$SD) ($p < 0.0001$, one-way ANOVA). No difference was found between the AGV of the WT afferents and the “normal-looking” afferents in the GluA3^{KO} ($p > 0.005$, one-way ANOVA pair comparison). In addition, we found that the swollen afferents in GluA3^{KO} (circularity mean = 0.8 $\pm$ 0.1 $\pm$ SD; roundness mean = 0.74 $\pm$ 0.13 $\pm$SD) were significantly more circular and round than the “normal-looking” afferents in the KO (circularity mean = 0.6 $\pm$ 0.11 $\pm$ SD; roundness mean = 0.44 $\pm$ 0.15 $\pm$SD) or the GluA3^{WT} afferents (circularity mean = 0.43 $\pm$ 0.1 $\pm$ SD; roundness mean = 0.41 $\pm$ 0.17 $\pm$SD) ($p < 0.0001$, one-way ANOVA). A paired comparison between the “normal-looking” afferents in the KO and the GluA3^{WT} afferents showed that the formers were more circular ($p = 0.045$). In this analysis, we did not separate the data between modiolar and pillar side synapses. The observation of vacuole-associated Type I

afferent swellings increased in the female KO at P60 and were also observed in the apex of the cochlear spiral (not shown). Swelling of afferent terminals suggests glutamate excitotoxicity and synaptophathy in GluA3^{KO}, reminiscent of noise-exposed or ischemic tissue from animals with intact GluA3 (Robertson 1983; Puel et al., 1994, 1998). Vacuoles or afferent swellings were not observed in female GluA3^{WT} mice in ambient or in either genotype raised in quiet, in which only normal-looking synapses were observed (**Fig. 7A-C, H-I, J-K**). Our results show chronic synaptopathy appearing ultra-structurally and physiologically before potential deafferentation of the IHC in female GluA3^{KO} mice raised in ambient sound.

Pre- and post-synaptic ultrastructural features of IHC-ribbon synapses in 5-week-old female mice raised in quiet.

Previously, we reported that P35 male GluA3^{KO} mice raised in ambient sound levels had normal ABR and a similar number of paired IHC-ribbon synapses. However, those male KO mice showed defective differentiation of modiolar-side and pillar-side pre- and post-synaptic ultrastructural specializations (Rutherford et al., 2023). Due to the abundance of swollen afferents in the female GluA3^{KO} in ambient, we performed morphometric analysis of the pre- and post-synaptic structure of the modiolar- and pillar- side IHC-ribbon synapses in 5-week GluA3^{WT} and GluA3^{KO} mice raised in quiet. This analysis of synapses from mice raised in quiet allows us to determine structural alterations associated with increased synaptic vulnerability in louder sound environments.

<u>Ultrastructure in C57BL/6 GluA3^{WT} in quiet</u>

Thirty-five IHC-ribbon synapses of female GluA3^{WT} mice were analyzed in three dimensions (3D) using ultrathin serial sections (on average, 10 ultrathin sections per PSD). Of this total, 24 synapses were on the modiolar side and 11 on the pillar side of IHCs. In our sample of modiolar-side synapses, 19 had one single ribbon, whereas 5 had two ribbons. All pillar-side synapses had

only one ribbon. We did not find differences in PSD surface area or volume between the modiolar synapses with one or two ribbons, so data was combined. Next, we compared the PSD surface area and volume between modiolar side and pillar side and did not observe any difference in GluA3^{WT} (surface area p = 0.52; volume p = 0.10, unpaired t-test) (**Figs. 7 and 8A top; Table 1**). In contrast, male GluA3^{WT} PSDs were larger on the modiolar side (Rutherford et al., 2023). Data from single ultrathin sections showed that the PSD linear length was similar between the modiolar- and pillar-side synapses (p = 0.93, Mann-Whitney test) (**Fig. 8B top; Table 2**).

We next compared the presynaptic ribbon surface area and volume between modiolar- and pillar-side synapses in GluA3^{WT} (**Fig. 8A top; Table 1**). The ribbon surface area of the modiolar-side was significantly larger than the pillar-side (p = 0.03, unpaired t-test). In contrast, ribbon volume was similar (p = 0.56).

Analysis of the presynaptic ribbon major and minor axes showed that the major axis of modiolar-side ribbons was not significantly different from the pillar side (p = 0.06, unpaired t-test) (**Fig. 8B top; Table 2)**, in contrast to GluA3^{WT} males (Rutherford et al., 2023). The minor axis of modiolar-side ribbons was significantly smaller than the pillar side (p = <0.0001, unpaired t-test) (**Fig. 8B top; Table 2**). Moreover, ribbons of the modiolar-side were less circular (p = 0.0002, unpaired t-test) and more elliptical (p < 0.0001 unpaired t-test) than those on the pillar side (**Fig.8B top; Table 2**), as was observed in the males. Analysis of synaptic vesicles (SVs) showed that those of the modiolar-side were larger than those of the pillar-side (p = 0.0005, Mann-Whitney test) (**Fig. 8B top; Table 2**), as in the males (Rutherford et al., 2023).

<u>Ultrastructure in C57BL/6 GluA3^{KO} in quiet</u>

From GluA3^{KO}, 35 IHC-ribbon synapses were analyzed in 3D with serial ultrathin sections (on average, 10 ultrathin sections per PSD). Of this total, 24 were on the modiolar side and 11 on the pillar side of the IHCs. Seventeen synapses on the modiolar-side had one ribbon, whereas 7 had double ribbons. In contrast to GluA3^{WT}, 3 synapses on the pillar-side in GluA3^{KO} mice had 2 ribbons, whereas 8 had a single ribbon. We did not find differences in PSD surface area or volume between the modiolar or pillar synapses with one or two ribbons, so data were combined. We then compared the PSD surface area and volume between the modiolar and pillar sides (unpaired t-test unless noted). Similar to the GluA3^{WT}, there was no significant difference in the PSD surface area ($p = 0.16$, unpaired t-test) or volume ($p = 0.31$) (**Fig. 8A bottom; Table 1**). Unlike the GluA3^{WT}, the PSD length was significantly greater on the modiolar than on the pillar side ($p = 0.028$, Mann-Whitney test) (**Fig. 8B bottom; Table 2**).

The analysis of presynaptic ribbon surface area showed that those on the modiolar side had significantly larger surface area than those on the pillar side ($p = 0.007$, unpaired t-test) (**Fig. 8A bottom; Table 1**). In contrast, ribbon volume was similar between the modiolar and pillar sides ($p = 0.12$) (**Fig. 8A bottom; Table 1**).

Like GluA3^{WT} females, the major axis was similar between the modiolar- and pillar-side ribbons ($p = 0.08$, unpaired t-test) (**Fig. 8B bottom; Table 2**). In contrast to GluA3^{WT} mice, the minor axis was similar between the ribbons of the modiolar- and pillar-side synapses ($p = 0.15$) (**Fig. 8B bottom; Table 2**). Pillar-side ribbons were more circular ($p = 0.001$, unpaired t-test) and round ($p = 0.005$) than modiolar-side ribbons (**Fig. 8B bottom; Table 2**), but the difference was less significant than in the GluA3^{WT}. The analysis of the SVs size on modiolar- and pillar-side synapses showed that they were similar ($p = 0.63$, Mann-Whitney test) (**Fig. 8B; Table 2**).

SV size and ribbon shape were altered in the 5-week-old female GluA3^{KO} mice in quiet.

Next, we compared the pre- and post-synaptic ultrastructural features on the modiolar- and pillar-side synapses between genotypes (unpaired t-test in all the comparisons). The PSD surface area and volume were similar on the modiolar (surface area p = 0.43; volume p = 0.16) and pillar side synapses (surface area p = 0.78; volume p = 0.74) between GluA3^{KO} and GluA3^{WT} mice (**Fig. 9A left**). No differences in PSD length were observed between genotypes (modiolar p = 0.68; pillar p = 0.11) (**Fig. 9B top left**).

Synaptic ribbon surface area on the modiolar side was significantly reduced in GluA3^{KO} compared to GluA3^{WT} (p = 0.0096). In comparison, the surface area on the pillar side was similar between the genotypes (p = 0.073) (**Fig. 9A right**). Ribbon volumes on the modiolar side were similar between GluA3^{KO} and GluA3^{WT} (p = 0.25), whereas, on the pillar side, the ribbon volumes of GluA3^{KO} were significantly smaller than GluA3^{WT} (p = 0.029) (**Fig. 9A right**). There was no significant difference in ribbon major axes on the modiolar- or pillar-side synapses between the GluA3^{WT} and GluA3^{KO} (modiolar: p = 0.34, pillar: p = 0.56). In contrast, the ribbon minor axes of GluA3^{KO} modiolar side synapses were larger than those of the GluA3^{WT} (p = 0.018). The minor axes of pillar side synapses were the same between genotypes (p = 0.12) (**Fig. 9B center**). The ribbon of modiolar side synapses of GluA3^{KO} was more circular and rounder than in GluA3^{WT} (circularity, p = 0.049, roundness, p = 0.010). On pillar-side synapses, ribbon circularity and roundness were similar between the genotypes (circularity, p = 0.90, roundness, p = 0.36) (**Fig. 9B bottom**). While SV size on the modiolar side was similar between genotypes, those on the pillar side were significantly larger in GluA3^{KO} mice (modiolar, p = 0.059, pillar, p < 0.0001) (**Fig. 9B top right**).

Next, we designed an analysis in 2D to determine the ribbon shape by dividing the major to the minor axis (see Material and Methods); this ratio is independent of size. The schematic diagram in Figure 9C explains that round ribbons (shown in red) have equal lengths on the major and minor axes. In contrast, elliptical ribbons (shown in purple) have a major axis longer than the minor. The pie charts show the variability in ribbon shape from round to elongated as a total (modiolar + pillar) and then separated by modiolar- and pillar-side ribbons (**Fig. 9C**). Overall, ribbons in GluA3^{WT} and GluA3^{KO} varied in shape from round to elongated; however, the KO ribbons were less elongated and rounder (**Fig. 9C top pie chart**). When comparing the shapes separated by modiolar and pillar, data showed that 18% of the modiolar-side ribbons in the GluA3^{WT} mice were elliptical, although a larger percentage (36%) were round. In the WT pillar-side ribbons, the large majority (60%) were round, and the elliptical ribbons were not observed (**Fig. 9C**). In the GluA3^{KO}, in contrast to the GluA3^{WT}, we did not find the most elliptical category within the modiolar-side ribbons. In the KO, 15% of modiolar ribbons were round, and the rest (85%) were between elliptical and round. Almost half (47%) of pillar-side ribbons in the GluA3^{KO} were round, and the others had intermediary shapes (**Fig. 9C**).

In summary, our ultrastructural data from 5-week-old female mice showed that in contrast to the GluA3^{WT}, the PSD length of the GluA3^{KO} modiolar and pillar side synapses differed (smaller in the pillar). However, this difference was not significant when compared between genotypes. In addition, we observed that the shape of the pre-synaptic ribbons of both synapse types and the SV size of pillar-side synapses were altered in the female GluA3^{KO} mice in quiet.

Type I afferent terminals in the GluA3^{KO} mice in quiet had a decrease in mitochondria content.

Mitochondria often occupy neurons and have many protective properties, including their role in calcium buffering (Duchen, 2000; Wang et al., 2019; Matuz-Mares et al., 2022; Verma et al., 2022). To analyze the presence of mitochondria in the afferent terminals of Type I SGNs on IHCs, we quantified the number and percentage of mitochondria in modiolar- and pillar-side afferents of GluA3^{WT} and GluA3^{KO} mice in quiet (**Fig. 9 left**). In GluA3^{WT}, out of the total afferent terminals analyzed along modiolar and pillar side of hair cells, 20% of modiolar-side afferent terminals were without mitochondria, whereas 43% had (range: 1 - 9 mitochondria per afferent; median: 3). In contrast, all the pillar-side afferent terminals (representing 37% of the total) had mitochondria (range: 1 - 8 mitochondria per afferent; median: 4). The analysis of the GluA3^{KO} shows that out of the total, 26% of the modiolar-side afferents lacked mitochondria, whereas most had them (42% of the total; range: 1 - 8 mitochondria per afferent; median: 2). Of the pillar-side afferents, we found that in contrast to the GluA3^{WT}, 7% lacked mitochondria whereas 25% had them (range: 1 - 8 mitochondria per afferent; median: 4). Overall, we find that in GluA3^{KO} mice, there is an increase in the percentage of both modiolar- and pillar-side afferents lacking mitochondria compared to GluA3^{WT} mice.

Within the afferents with mitochondria, either in GluA3^{WT} or GluA3^{KO} mice, the number of mitochondria varied from 1 to 9. Because the median was around 3 on average, we determined how many afferents had fewer mitochondria below the median (n = 1 - 2 mitochondria per afferent) and how many had above the median (more than 3) (**Fig. 9 right**). In GluA3^{WT}, the percentage of modiolar-side afferent terminals with a lower and higher number of mitochondria was similar (25% and 28%, respectively). In contrast, only a small percentage (6%) of pillar-side afferent terminals had a lower number of mitochondria, whereas the majority (41 %) had a higher number. In the GluA3^{KO}, the percentage of modiolar-side afferents with one or two mitochondria was larger than those with more than three (38% and 24%, respectively). In pillar-side afferents, 14% had one or

two mitochondria, while the rest (24%) had more than three. When comparing GluA3^{WT} and GluA3^{KO} data, we found that in the GluA3^{KO,} there was an increase in the number of modiolar and pillar side afferents with a low number of mitochondria. A larger percentage of afferent terminals without or with a lower number of mitochondria in the female GluA3^{KO} could contribute to a higher IHC-ribbon synapse vulnerability to ambient sound levels.

Discussion

In the present study, we analyzed the role of the GluA3 subunit on sound encoding, AMPAR subunit composition, and pre-and post-synaptic ultrastructure of IHC-ribbon synapses in female mice in ambient and quiet sound conditions. Our study shows that in the female GluA3^{KO} mice, only ambient background sound levels lead to early hearing impairment (**Fig.1 and 2**), an increase in the number of ribbonless synapses (**Fig. 3**), and afferent terminal swellings (**Fig. 7**), suggesting excitotoxicity. The excitotoxicity in afferent terminals of female GluA3^{KO} potentially results from an increase in the Ca^{2+} permeability through the AMPAR channel as a consequence of the higher GluA4:GluA2 ratio and altered intrasynaptic distribution of the subunits within the postsynaptic structure of IHC-ribbon synapses (**Fig. 4, 5 and 6**). In addition, we find that GluA3 plays a crucial role in maintaining the morphology of pre-synaptic ribbons and SVs, and of afferent terminal mitochondria content in both modiolar- and pillar-side synapses (**Fig. 8-9**), all indicating that GluA3 is necessary for the development and maturation of IHC-ribbon synapses. Together, our results indicate that the AMPAR subunit GluA3 is required to prevent excitotoxicity in ambient sound levels and maintain the normal structure of IHC synapses in young female mice.

Lack of GluA3 in females increases IHC-ribbon synapse vulnerability to ambient sound

We recently found that 5-week-old GluA3^{KO} males raised in ambient sound levels have normal hearing sensitivity, measured by ABR click and pure-tone thresholds and wave-1 amplitude (Rutherford et al., 2023). The male GluA3^{KO} mice do not show hearing impairment until they reach 2 months of age (García-Hernández et al., 2017). Here, we show that female GluA3^{KO} raised in the same ambient background sound levels have a decreased wave-1 amplitude at 5 weeks of age that persists up to at least 3 months (**Fig. 1**). This early decrease in wave-1 amplitude suggests reduced SGN synchrony in the female GluA3^{KO} mice. Interestingly, our data also show that the increased vulnerability of the female GluA3^{KO} to ambient sound can be prevented at least up to 3 months of age if mice are raised in much quieter sound environments (**Fig. 1**). All of this suggests that female GluA3^{KO} mice show a greater vulnerability than males to changes in sound environment.

Among the potential contributors to increased hearing loss vulnerability in the absence of GluA3 is a change in AMPAR subunit composition, specifically less GluA2 or more GluA4 (**Fig. 3 - 6**), likely to increase the abundance of Ca^{+2}-permeable AMPARs (CP-AMPARs) at the IHC-ribbon synapse. AMPARs underlie fast excitatory synaptic transmission at IHC-ribbon synapses (Ruel et al., 1999; Glowatzki and Fuchs, 2002). The activity of AMPARs is crucial for the normal physiology of synapses and, on the other hand, for the induction of excitotoxicity (Puel et al., 1998; Ruel et al., 2000). Several studies have shown that noise-induced hearing loss can produce excitotoxicity through excessive release of glutamate and subsequent activation of AMPARs, specifically Ca^{2+}-permeable AMPARs (Kim et al., 2019; Hu et al., 2020). AMPARs at mature IHC-ribbon synapses are assembled as tetramers comprised of different combinations of GluA2 – 4 subunits; homotetramers can exist but are less stable energetically (Rossmann et al., 2011; Zhao et al., 2017). Calcium conductance of AMPARs varies depending on the presence of GluA2 subunits in the tetrameric complex, and AMPARs lacking GluA2 subunits are Ca^{+2} permeable

(Hollmann et al., 1991; Geiger et al., 1995). Immunoreactivity for GluA2/3 or GluA2 is widely reported as present at all, or nearly all, IHC-ribbon synapses (Khimich et al., 2005; Meyer et al., 2009; Liberman et al., 2011). The presence of GluA2 presumably reduces overall synaptic Ca^{2+} influx and vulnerability to glutamate excitotoxicity. Nonetheless, glutamate excitotoxicity underlies noise-induced cochlear synaptopathy, and recent studies in rats and mice have shown the existence of apparently GluA2-lacking nanodomains presumably containing CP-AMPARs within postsynaptic densities and that antagonizing these CP-AMPARs can prevent noise-induced synaptopathy (Sebe et al., 2017; Hu et al., 2020).

While the full complement of AMPAR pore-forming and auxiliary subunits functioning at IHC-ribbon synapses is still undetermined, in the absence of GluA3 and GluA1 (Rutherford et al., 2023), GluA2/4, GluA2/2, and GluA4/4 are the only possible pore-forming dimers to dimerize into the tetrameric AMPAR complex. In our study, we find the number of paired synapses (i.e., a presynaptic ribbon paired with postsynaptic GluA2 and GluA4) was similar between $GluA3^{WT}$ and $GluA3^{KO}$ female mice in both ambient and quiet rearing by 5 weeks (**Fig. 3**). However, the number of lone ribbons and ribbonless synapses was significantly greater in the KO, but interestingly, only if raised in ambient sound levels (**Fig. 3**). GluA2-lacking synapses were not observed in $GluA3^{WT}$ and in less than 2% of synapses in $GluA3^{KO}$ in quiet or ambient. GluA4-lacking synapses (i.e., a presynaptic ribbon paired with postsynaptic GluA2 only) were not observed in quiet in either genotype. Ambient sound increased the occurrence of GluA4-lacking synapses in both genotypes, with significantly more in $GluA3^{WT}$ than $GluA3^{KO}$ (~ 30% of synapses in some images from the 10 kHz region (**Fig. 3**). Thus, ambient sound appears to induce a shift toward GluA2-only synapses in $GluA3^{WT}$ and toward unpaired pre- and post-synaptic puncta in $GluA3^{KO}$. Both genotypes had unpaired synapses when reared in ambient sound, but ribbonless synapses containing GluA2 and GluA4 were more abundant in $GluA3^{KO}$ (~ 10%) than $GluA3^{WT}$ (~ 5%). As

well, these ribbonless synapses in GluA3^{WT} tended to have greater GluA4:GluA2 ratios (implied Ca^{2+} permeability) than the paired synapses in the same images but not in GluA3^{KO} (**Fig. 4**). If the presence of the ribbon in GluA3^{WT} is associated with AMPARs having relatively less Ca^{2+} permeability, one implication is that ambient sound recruits GluA2 to ribbon synapses, somehow making them relatively less vulnerable to excitotoxicity.

In GluA3^{KO} females, as in males, the ribbon-occupied synapses (i.e., paired synapses) are already elevated in the GluA4:GluA2 ratio, suggesting an increase in the relative abundance of GluA2-lacking CP-AMPARs (**Fig. 4**). This may lead to excessive influx of Na^{+} and Ca^{++} into the Type I afferent terminals, increasing their intracellular concentration. Intriguingly, the increase in the GluA4:GluA2 ratio occurred in ambient and in quiet conditions, but the change was larger in ambient (~ 100% increase in ambient vs. ~ 60% increase in quiet). Remarkably, only in the female KO in ambient conditions did we observe afferent swellings (**Fig. 7**), which were similar to but much less extensive than those reported after noise exposure or following cochlear perfusion with excitotoxic glutamate receptor agonists (Robertson, 1983; Puel et al., 1998). Thus, the further increase in the GluA4:GluA2 ratio between quiet and ambient seems sufficient to trigger a slowly progressing excitotoxicity in the afferent terminals. Structural features of swollen afferents include missing mitochondria, swollen endoplasmic reticulum, and decreased cytoplasm electron-density. Some swellings had a PSD in opposition to a pre-synaptic ribbon, while others lacked the ribbon. The former would likely appear as a normal paired synapse in confocal imaging, and the latter would be considered a ribbonless synapse. Altogether, our results show the existence of chronic ultra-structural and physiological ambient sound-induced synaptopathy long before the synapses degenerate in the female GluA3^{KO} cochlea.

Molecular and ultrastructural changes are already present in quiet

Even in the absence of ambient sound, we found differences between GluA3^{WT} and GluA3^{KO}. In addition to the greater overall GluA4:GluA2 fluorescence ratios in GluA3^{KO} synapses, we find an altered intrasynaptic distribution of ratios (females in quiet, **Fig. 5 - 6**). In GluA3^{WT}, the ratios tended to peak 200 – 400 nm from the synapse center, which would be closer to the perimeter of the PSD as measured in TEM (**Fig. 7**). This peak was less pronounced in GluA3^{KO} because ratios tended to be greater near the synapse center in GluA3^{KO} than in GluA3^{WT}. Electron tomography has localized SVs morphologically docked to the presynaptic membrane only within ~ 100 nm of where the synaptic ribbon is anchored to the active zone, suggesting exocytosis may be limited to within 100 nm from the ribbon (Chakrabarti et al., 2022). More GluA2-lacking and presumably CP-AMPARs residing closer to the ribbon would likely increase the probability of their activation after presynaptic glutamate release, perhaps leading to excitotoxicity in female GluA3^{KO} mice raised in ambient sound levels.

Postsynaptic calcium homeostasis is crucial to protect synapses from excitotoxic insult (Verma et al., 2022), for which mitochondria play an important role (Duchen, 2000; Verma et al., 2022). Reduced calcium buffering by mitochondria in the afferent terminals of GluA3^{KO} females could contribute to afferent terminal swellings and excitotoxicity. Structural studies in cats and mice indicated that pillar-side terminals contained more and larger mitochondria than modiolar-side terminals (Liberman, 1980; Moverman et al., 2023). This difference in mitochondrial content might increase the vulnerability of afferent terminals on the modiolar side to damage after noise exposure. In our study, we find a similar trend in the female C57BL/6 GluA3^{WT} mice raised in quiet, where pillar-side terminals contained more mitochondria than modiolar-side terminals (**Fig. 9**) In addition, we identified a ~20% of modiolar afferents without mitochondria at the afferent terminals in the GluA3^{WT}. However, in the GluA3^{KO} females, we find an increase in afferent

terminals of both modiolar- and pillar-side synapses, either without or with a low number of mitochondria (**Fig. 9**). The afferent terminals of female GluA3^{KO} raised in quiet are structurally and functionally asymptomatic, but these results suggest less Ca^{2+} buffering capacity, which may increase vulnerability. Postsynaptic mitochondria are critical to the development, plasticity, and maintenance of synaptic inputs (Thomas et al., 2023). Although the link between reduced mitochondrial content and the absence of GluA3 is unclear, our results suggest GluA3 may influence modiolar- and pillar-side differences in mitochondrial content that emerge during development. Altogether, the altered synaptic AMPAR subunit composition and the decrease in mitochondria content at afferent terminals of the female GluA3^{KO} in quiet, while being asymptomatic, could increase the synapse vulnerability if mice are raised in louder ambient sound levels, as we find in this study.

Lack of modiolar-pillar spatial gradient of synaptic structural heterogeneity at IHC-ribbon synapses in GluA3^{KO} mice

Our recent ultrastructural and imaging study of cochlear ribbon synapses in 5-week-old male GluA3^{KO} mice included dysregulation of GluA2 and GluA4 subunit relative abundance and alterations in pre- and post-synaptic ultrastructure associated with an increased vulnerability to glutamatergic synaptopathy at ambient, background levels of sound (Rutherford et al., 2023). These structural and molecular alterations at the cochlear ribbon synapses of pre-symptomatic 5-week-old male GluA3^{KO} mice appear to be pathological, preceding the reduction in ABR wave-1 amplitudes observed at 2-months of age (Garcia-Hernández et al., 2017). Among the structural alterations, we found that IHC modiolar-pillar differences were eliminated or reversed in the male GluA3^{KO}. Specifically, the major axis of the modiolar-side ribbons was smaller in GluA3^{KO} males.

The SVs were also larger on both the modiolar and pillar sides compared to the GluA3^{WT}. (Rutherford et al., 2023). Here, our structural analysis of 5-week-old female GluA3^{WT} and GluA3^{KO} in ambient and quiet showed that only the female KOs raised in ambient sound levels had decreased wave-1 amplitude and the characteristic Type I terminal swellings, indicating functional and structural synaptopathy (**Fig. 1, 2 and 7**). Thus, we reasoned that analyzing the structure of the IHC-ribbon synapses of the female KOs in quiet would provide a unique opportunity to identify pre-symptomatic features associated with an increased vulnerability to glutamatergic synaptopathy at ambient sound levels.

Our ultrastructural analysis of the IHC-ribbon synapses of females in quiet showed that in C57BL/6 GluA3^{WT} mice, the PSD and ribbon major axis lengths of the modiolar and pillar side synapses were similar (**Fig. 8 and 9**), differing from what we and others found in WT C57BL/6 or CBA/CaJ males (Rutherford et al., 2023; Liberman et al., 2011) or in a (presumably male) cat raised in a low-noise chamber (Liberman, 1980), where modiolar side ribbons are larger. In GluA3^{KO} females, the modiolar-side ribbons widened due to a significant increase in the minor axis length, while pillar ribbons tended to be more elongated due to the reduced minor axis length, and no difference was observed in the ribbon major axis (**Fig. 8 and 9**). Similar to the male GluA3^{WT}, the SVs were larger on the modiolar side in female GluA3^{WT}. In GluA3^{KO}, the SVs on modiolar and pilar side synapses did not differ in size because SVs on the pillar side were larger. The length of the PSD in female GluA3^{KO} mice was larger in modiolar-side synapses compared to pillar side (**Fig. 8 and 9**). Altogether, we find that lack of GluA3 alters pre- and postsynaptic features of both modiolar- and pillar-side synapses. However, we were surprised that the effects in the female GluA3^{KO} were less prominent than in the males, especially the structural alterations of the modiolar side ribbons. This could be because we analyzed the females reared in the quiet, while our previous study assessed male mice raised in ambient sound. In any case, the spatial

gradient of modiolar- and pillar-side synapse heterogeneity seems weaker in females. Nonetheless, our ultrastructural analysis in females supports the role of GluA3 in maintaining pre- and post-synaptic structural features. We propose that this occurs through an unknown trans-synaptic mechanism during development at IHC-ribbon synapses in the cochlea and the endbulb of Held synapses in the cochlear nucleus (García-Hernández et al., 2017; Antunes et al., 2020; Rutherford et al., 2023). AMPAR subunits in the cochlea may interact with the trans-synaptic adhesion proteins Neuroligins and Neurexins, which could also interact with presynaptic proteins and voltage-gated Ca^{2+} channels at IHC-ribbon synapses (Arac et al., 2007; Luo et al., 2020; Ramirez et al., 2022).

Why are females lacking GluA3 more vulnerable to ambient sound levels than males?

Studies in mice, chinchillas, and humans reported that males are more vulnerable to noise-induced hearing loss than females (McFadden et al., 2000; Milon et al., 2018; Szanto and Ionescu, 1983; Shuster et al., 2021). Here, we show that the absence of the GluA3 AMPAR subunit increases the vulnerability of the female mice to ambient sound levels. Taken together, our data suggests that the decreased vulnerability observed in female mice requires the presence of GluA3 at the IHC-ribbon synapse. The effect of GluA3's absence on increasing excitotoxicity in female mice reared in ambient sound may be indirect due to the decrease in GluA2 at the synapse **Fig. 3 - 6**); however, this decrease in GluA2 was observed also in male $GluA3^{KO}$ mice reared in ambient sound (Rutherford et al., 2023). Perhaps females have a unique requirement for GluA3, or males have a unique means of resisting excitotoxicity in its absence. GluA3 and GluA2 form the most predominant dimers in the brain (Rossmann et al., 2011; Zhao et al., 2017), and we assume this biophysical property extends to the inner ear, although this remains to be shown directly. We speculate that loss of GluA3 results in decreased trafficking of GluA2 to the synapse

since *Gria2* RNA levels were not reduced in *Gria3*^{KO} mice (Rutherford et al., 2023). Still, it remains unclear why the 5-week-old GluA3^{KO} male mice did not exhibit a reduction in ABR wave-1 amplitudes or elevation of ABR thresholds. Recently, we showed that spiral ganglion neurons (SGN) from female mice have a two-fold higher expression of *Gria3* mRNA and larger ABR wave-1 amplitudes than male mice (Lozier et al., 2023). While *Gria2* and *Gria4* are located on autosomes, *Gria3* is on the X chromosome (Mahadevaiah et al., 2009). Therefore, it is possible that females have more GluA3 due to incomplete X-inactivation in some or all SGNs, leading to increased gene dosage (Carrel and Willard, 2005; Berletch et al., 2015). If so, knocking out *Gria3* could have a greater impact on the female than the male IHC-ribbon synapse.

Material and Methods

Animals

In this study, a total of 57 female C57BL/6 wild type (GluA3^{WT}, n= 26) and GluA3-knockout (GluA3^{KO}, n= 31) mice from two different colonies were used between postnatal days 20 (P20, 3-weeks) to 90 (P90, 13-weeks). The generation of the GluA3^{KO} mice has been previously described (García-Hernández et al., 2017; Rubio et al., 2017). Mice were raised up to P20 in quiet sound pressure levels conditions (40 - 55 dB SPL, 100 Hz – 8.3 kHz, general audible range for humans, measured with an audiometer, General Tools & Instruments LLC; 10 dB SPL, 3 kHz–90 kHz, mouse hearing range, Sensory Sentinel, Turner Scientific, Jacksonville, IL). One group of GluA3^{WT} (n= 13) and *GluA3*^{KO} (n= 14) mice were maintained in the same quiet conditions until P90 (**Fig. 1A**). A second group of mice (GluA3^{WT} n= 13) and (GluA3^{KO} n= 17) were moved at P20 to a room facility with ambient sound pressure levels (55-75 dB SPL,100 Hz – 8.3 kHz, general audible range for humans measured with an audiometer; 20 - 40 dB SPL, 3 kHz–90 kHz, mouse hearing range, Sensory Sentinel) and maintained until they reached P90 (**Fig. 1A**). Both mouse

groups were reared in a 12-hour light/12-hour dark daily photoperiod and were fed *ad libitum*. Auditory brainstem recordings (ABRs) were collected at four postnatal days: P20, P35, P60, and P90. Cochleae were dissected from P35 mice and used for further experiments (**Fig. 1A**). All experimental procedures were per the National Institute of Health guidelines and approved by the University of Pittsburgh Institutional Animal Care and Use Committee.

Auditory Brainstem Recordings (ABRs)

At least 10-15 GluA3^{WT} and GluA3^{KO} mice from each animal group (quiet and ambient) and age group were used for ABRs. During the ABRs, mice were kept anesthetized with isoflurane (3% induction and 1.5% maintenance), and the internal temperature was monitored with a thermometer (J/K/T Thermocouple, Kent Scientific Corporation) that was kept constant between 37-38 ˚C using isothermal heat pads. Open-field ABRs and analysis were performed as described in Lozier et al. (2023). Briefly, ABRs were recorded in a sound attenuation chamber inside a Faraday cage. The speaker was calibrated in the chamber using a microphone (PCB electronics, model no. 377C01, Depew, NY) placed 10 cm from the multi-field magnetic speaker (MF1, Tucker-Davis Technologies (TDT), Alachua, FL), which was the same distance as the mouse's external ear to the speaker during experiments. For ABR recordings, needle electrodes were placed subcutaneously at the vertex of the scalp and below the pinna of both the tested (ipsilateral) and contralateral ears. Clicks (1 ms) or pure tones of 4, 8, 12, 16, 24, and 32 kHz (0.5 ms) stimuli were presented from 90 dB to 10 dB in decreasing steps of 5 dB at 21 sweeps with an interstimulus interval of 47.6 ms. All the recordings' responses were averaged over 512 sweeps, amplified, digitized, and transferred via an optical port to the RZ6 processor. ABR click, and pure tone thresholds were determined as the lowest intensity level (in dB SPL) at which reproducible peaks were visible. The clicks wave I amplitude (in μV) was determined as the difference between the peak and subsequent trough.

Immunofluorescence

A total of 9 female mice (GluA3^{WT} n = 4; GluA3^{KO} n = 5) at 5 weeks of age, raised in either ambient sound (ambient group) or low-level sound (quiet group) were anesthetized with ketamine (60 mg/kg) and xylazine (6.5 mg/kg), then perfused intravascularly for 10 minutes with fixative consisting of 4% paraformaldehyde (PFA) in 0.1M phosphate buffer (PB), pH = 7.2. Temporal bones were then isolated from the skull, the stapes was removed, the oval and round window membranes were punctured, and a hole was opened at the apex of the cochlear bone near the helicotrema. Each cochlea was perfused with fixative through the oval window while bathing in a dish of fixative. After postfixation for 45 minutes in the dish on top of an ice pack, the cochleae were rinsed in 0.1M phosphate-buffered saline (PBS) and then shipped to Washington University in St. Louis overnight in PB supplemented with 5% glycerol.

GluA3^{WT} and GluA3^{KO} cochleae were batch processed in parallel using the same reagent solutions in two separate groups, one raised in ambient background sound and the other raised in quiet background sound levels. After rinsing in PB, each temporal bone was decalcified in 50 mL of PB supplemented with 10% EDTA for 2 hours at room temperature on a rocker. After removing the outer shell of the cochlea and peeling away the lateral wall, the spiral containing the organ of Corti, osseous spiral lamina, and spiral ganglion was isolated and cut into apical-cochlear, middle-cochlear, and basal-cochlear pieces for wholemount immunolabeling as previously described (Jing et al., 2013; Ohn et al., 2016; Sebe et al., 2017; Kim et al., 2019; Hu et al., 2020; Rutherford et al., 2023). To permeabilize the tissue and to block non-specific binding of antibodies, the samples were immersed overnight at 4°C in 100 µL of blocking buffer (0.3% Triton X-100 and 16% normal horse serum in PBS) in a 9-well Pyrex glass plate. To label presynaptic ribbons (CtBP2/Ribeye) and postsynaptic AMPA-type glutamate receptor subunits

(GluA2, GluA3, and GluA4), primary antibodies were diluted in blocking buffer (1:400) and samples were incubated in the 9-well plates with 100 μL per plate overnight at 4°C: CtBP2 mouse IgG1 (BD Biosciences 612044; RRID:AB_399431), GluA2 mouse IgG2a (Millipore MAB397; RRID:AB_2113875), GluA3 goat (Santa Cruz Biotechnology SC7612), and GluA4 rabbit (Millipore AB1508; RRID:AB_90711). After rinsing 3 times in wash buffer (PBS supplemented with 0.3% Triton-X), samples were incubated for 1 hour at room temperature in species-appropriate secondary antibodies diluted in blocking buffer (1:100). Secondary antibodies were pre-conjugated to Alexa Fluor (Life Tech.) fluorophores excited by 488, 555, or 647 nm light. After rinsing 3 times in wash buffer and PBS, the 3 pieces from each cochlea were mounted in Mowöl between a microscope slide and coverslips (#1.5, Zeiss). Slides were kept at 4°C until imaging.

Conventional Confocal Microscopy and Image Analysis

Confocal volumes were acquired with 12-bit images, 100 μm wide containing approximately 12 IHCs, on a Zeiss LSM 700 with a 63X 1.4 NA oil objective lens with a Z-step of 0.37 μm and pixel size of 50 nm in X and Y, and a pinhole setting of 1 AU. We first surveyed the samples to determine the necessary laser power settings to collect all the images at a gain of 700 while avoiding pixel intensity saturation. Using identical acquisition settings across samples, we collected 3–4 images from the center of each of the 3 pieces (basal-, middle-, and apical-cochlear) near tonotopic characteristic frequencies of 10, 20, and 40 kHz (Müller et al., 2005). For display only, the brightness and contrast levels were adjusted linearly for visual clarity. Image analysis was performed on raw data.

The numbers of hair cells and synapses were counted and manually verified after semi-automated identification using Imaris software (Bitplane) to calculate the mean number of synapses per IHC per image. The observers were blinded to mouse genotype. For each group of images, group

means (± SD) were calculated across image means. Paired synapses were identified as juxtaposed puncta of presynaptic ribbons (Ribeye/CtBP2) and postsynaptic AMPA receptor patches (GluA2 and/or GluA4), which appear to partly overlap at confocal resolution (Rutherford, 2015). Unpaired (i.e., lone) ribbons were defined as Ribyeye/CtBP2 puncta located under inner hair cell nuclei, in the synaptic region, but lacking apposed GluA2 or GluA4 puncta. Inner hair cell nuclei were labelled with CtBP2/Ribeye because CtBP2 is a transcriptional co-repressor. For unpaired ribbons, we did not distinguish membrane-anchored from unanchored. Ribbonless synapses consisted of GluA2 and/or GluA4 puncta located in the synaptic region under the inner hair cell nuclei but lacking apposed presynaptic ribbons.

Pixels comprising puncta of synaptic fluorescence were segmented in 3D as 'surface' objects in Imaris using identical settings across image stacks, including the 'local contrast background subtraction' setting to automatically calculate the appropriate pixel-intensity threshold for each fluorescence channel in each image. This adaptive and automatically-calculated thresholding algorithm compensated for differences in overall luminance between image stacks that would affect the volume of segmented puncta if a fixed threshold was applied across images, and avoided the potential subjective bias of setting a user-defined arbitrary threshold value separately for each image. Intensity per synaptic punctum was calculated as the summation of pixel intensities within the surface object. To associate the intensities of puncta belonging to the same synapse, we generated surface objects from a 4th channel calculated in Imaris as the sum of the three channels (GluA2, 3, and 4; or CtBP2, GluA2, and GluA4). Each of these 4th-channel objects contained the entire synapse (presynaptic and postsynaptic elements). The summated pixel intensities for each of the three fluorescence channels were calculated within each synapse. Some synapses appeared to lack a presynaptic ribbon. The CtBP2 channel was used to make surface objects of ribbons. These ribbon objects were used to remove ribbonless synapses from

the 4th-channel objects by eliminating 4th-channel objects with centers further than 0.1 μm from the center of the nearest ribbon. The average density of synaptic fluorescence per image was calculated as median punctum intensity (a.u.) divided by median punctum volume (μm^3) using surface objects calculated from corresponding individual fluorescence channels.

Airyscan Confocal Microscopy and Image Analysis

Airyscan volumes were acquired with 16-bit images, 46 μm wide containing approximately 5 IHCs, on a Zeiss LSM 880 Confocal with Airyscan, with a 100X 1.5 NA oil objective lens with a Z-step of 0.168 μm and pixel size of 26 nm in X and Y, and a pinhole setting of 1.5 AU. We collected stacks near tonotopic characteristic frequencies of 11, 20, 25, 38, 57, and 70 kHz using identical acquisition settings for all images. For display only, the brightness and contrast levels were adjusted linearly for visual clarity. Image analysis was performed on unadjusted data after Airyscan Processing.

To quantify changes in the relative abundance of GluA2 and GluA4 around individual synapses, 3-dimensional data was reduced to 1-dimensional normalized radial distributions of fluorescence density ratios around the synapse center. Analysis was performed blinded on the maximum intensity Z-projections for spatially-isolated synapses only (i.e., synapses having no overlap with other synapses XY or Z). The 2-dimensional centroid of the synaptic ribbon was defined as the synapse center. Radial distributions of normalized GluA4:GluA2 fluorescence density ratio as a function of distance from the synapse center were constructed with custom code in MATLAB Software. For each fluorescence channel, the sum of pixel intensities was calculated for a 3 x 3 pixel box (78 x 78 nm) centered on the ribbon centroid and then for 11 shells around the center box, with each shell expanding by 2 pixels (52 nm) on each side, such that the first shell was outlined by a square with dimensions of 7x7 pixels (182 x 182 nm) and the largest shell was

outlined by a square of 47x47 pixels (1,222 x 1,222 nm). For each shell, the area was calculated as the number of pixels, and the sum of pixel intensities was divided by the area to calculate the 'shell density' (intensity / area) for each fluorescence channel. For each isolated synapse in an image, the GluA4 : GluA2 radial distribution of the 'ratio of raw shell densities' was calculated as the blue shell density divided by the green shell density. The peak-normalized shell densities for each synapse were calculated by normalizing to the maximum shell density of each fluorescence channel such that each radial distribution of 'normalized shell density' peaked at value = 1. Then, the GluA4 : GluA2 'ratio of peak-normalized shell density' was calculated for each shell of each synapse by dividing the peak-normalized blue fluorescence shell density by the peak-normalized green fluorescence shell density. The average radial distribution for each image was calculated as the mean of the individuals. Group averages for $GluA3^{WT}$ and $GluA3^{KO}$ across CF regions were calculated as the mean of image-means. Shells were transformed to 26 nm bins and values were plotted as a function of increasing distance from the synapse center.

For the GluA4:GluA2 fluorescence ratios in nanodomains within synapses, each synapse was divided into 9 matrices of 13x13 pixels, with eight matrices around one center matrix centered on the ribbon centroid. Thus, each nanodomain matrix was 338^2 nm^2, and each 9-matrix synapse (3x3 matrices) covered an area of $1{,}014^2$ nm^2.

Transmission Electron Microscopy (TEM)

A total of 8 mice (2 per genotype either in quiet or ambient) at P35 were anesthetized with a mixture of ketamine (60 mg/kg) and xylazine (6.5 mg/kg) and were transcardially perfused with 0.1 M phosphate buffer (PB) pH = 7.2, followed by the fixative containing a mixture of 3% PFA and 1.5% glutaraldehyde in 0.1 M PB. Cochleae were dissected, fixed overnight at 4ºC, decalcified in 10% ethylenediaminetetraacetic acid (EDTA) for 24-48 hours at 4ºC, and processed

for osmication, dehydration, and embedding in epoxy resin using a similar method as previously described by Rutherford et al. (2023). A series of 15-20 ultrathin serial sections (70–80 nm in thickness) of the mid-cochlea (20kH) were cut with a Leica EM UC7 ultramicrotome and collected on single slot gold-gilded grids with formvar. The ultrathin sections were viewed under a transmission electron microscope (TEM; JEOL Ltd., Akishima Tokyo, Japan) and IHC-ribbon synapses of modiolar and pillar side were imaged (at x40,000 magnification) with an Orius SC200 CCD camera (Gatan Inc, Warrendale, PA, USA). Only, IHC-ribbon synapses that were clearly located either on the modiolar or the pillar side of the IHC were used for further ultrastructural analysis.

Three-Dimensional (3-D) Reconstructions and NIH Image-J Analysis of TEM micrographs

A total of 70 (GluA3^{WT} n= 35, GluA3^{KO} n= 35) IHC-ribbon synapses were used for the 3D analysis of the surface area and volume of the postsynaptic density (PSD) and the presynaptic ribbons. The TEM micrographs were calibrated, aligned, and reconstructed using the Reconstruct software (https://synapseweb.clm.utexas.edu/software-0; Fiala, 2005) as we previously described in Gómez-Nieto and Rubio (2009) and Rutherford et al. (2023). Additionally, in 27 (GluA3^{KO}) and 31 (GluA3^{WT}) IHC-ribbon synapses we analyzed the ribbon major and minor axes, the ribbon circularity and roundness, the PSD length, and synaptic vesicles (SVs) size from a representative TEM image of IHC-ribbon synapses using NIH ImageJ software (https://fiji.sc/) as described in Rutherford et al., (2023). SVs size was calculated as (Major diameter + Minor diameter)/2. Four to six SVs were analyzed per synapse, and the grand mean was used to compare the size of modiolar and pillar side SVs. We used the ratio of the ribbon's major and minor axes to analyze the ribbon shape. The major/minor axes ratio denotes the shapes of the ribbons regardless of the size. Each ribbon's ratio was classified into six groups, from 1-1.5 to >3.5. When a ribbon's major/minor axes ratio is one, it represents a round shape, while the higher major/minor ratio

represents a comparatively more elliptical shape. The presence of mitochondria in the afferent terminals of GluA3^{WT} and GluA3^{KO} in quiet was analyzed in 40 (modiolar: n= 25; pillar n= 15) and 43 (modiolar: n= 29; pillar n= 14) representative micrographs, respectively.

Representative electron micrographs of GluA3^{WT} (n= 20) and GluA3^{KO} (n= 38) in ambient were used to determine the average gray value (AGV settings: black = 0 and white = 255) per μm^2 of afferent terminal cytoplasm, and afferent circularity and roundness with NIH ImageJ.

Statistical Analysis

All the statistical analyses were conducted with GraphPad Prism software (version 9.4.1) or IGOR Pro (version 7.08, WaveMetrics). ABR comparisons were made with two-way mixed ANOVAs followed by Šidák's multiple comparisons. Two-tailed Mann–Whitney U-test with Holm- Šidák's correction for multiple comparisons or two-tailed unpaired t-tests were used to compare two independent groups. Two one-dimensional probability distributions were compared with the Kolmogorov–Smirnov (KS) test. For pairwise comparisons between more than two groups, one-way ANOVAs were used, followed by Tukey's post-hoc correction test. The Spearman rank-order correlation coefficient was used to test the strength of the association between the two variables. Statistical significance for all the tests was set to $p < 0.05$. Data are represented as mean ± standard deviation (± SD).

Acknowledgments

This work was supported by NIDCD DC013048 (MER) and NIDCD DC14712 (MAR).

Authors Contributions

M.E.R and M.A.R.: designed research, performed research, analyzed data, and wrote and edited the manuscript. I.P: performed research, analyzed data, wrote the first draft, and edited the manuscript. A.B.: analyzed data and edited the manuscript. M.X.: performed research and edited the manuscript. E.D.W.: analyzed data and edited the manuscript. B.V-G: designed and developed custom analytical tools.

Disclosure and competing interests' statement

The authors declare no competing financial interests.

References

Abdala C, Dhar S (2012) Maturation and aging of the human cochlea: a view through the DPOAE looking glass. *Journal of the Association for Research in Otolaryngology: JARO* 13:403–421

Antunes FM, Rubio ME, Kandler K (2020) Role of GluA3 AMPA Receptor Subunits in the Presynaptic and Postsynaptic Maturation of Synaptic Transmission and Plasticity of Endbulb-Bushy Cell Synapses in the Cochlear Nucleus. *The Journal of neuroscience: the official journal of the Society for Neuroscience* 40: 2471–2484

Araç D, Boucard AA, Ozkan E, Strop P, Newell E, Südhof TC, Brunger AT (2007) Structures of neuroligin-1 and the neuroligin-1/neurexin-1 beta complex reveal specific protein-protein and protein-Ca2+ interactions. *Neuron* 56: 992–1003

Bassani S, Folci A, Zapata J, Passafaro M (2013) AMPAR trafficking in synapse maturation and plasticity. Cell Mol Life Sci 70:4411-4430

Berletch JB, Ma W, Yang F, Shendure J, Noble WS, Disteche CM, Deng X (2015) Identification of genes escaping X inactivation by allelic expression analysis in a novel hybrid mouse model. *Data in brief* 5:761-769

Carrel L, Willard HF (2005) X-inactivation profile reveals extensive variability in X-linked gene expression in females. *Nature* 434:400-404

Chakrabarti R, Fung TS, Kang T, Elonkirjo PW, Suomalainen A, Usherwood EJ, Higgs HN (2022) Mitochondrial dysfunction triggers actin polymerization necessary for rapid glycolytic activation. *Journal of Cell Biology* 221

Duchen MR (2000) Mitochondria and calcium: from cell signalling to cell death. *The Journal of physiology* 529:57–68

Fiala JC (2005) Reconstruct: a free editor for serial section microscopy. *Journal of Microscopy* 218:52–61

García-Hernández S, Abe M, Sakimura K, Rubio ME (2017) Impaired auditory processing and altered structure of the endbulb of Held synapse in mice lacking the GluA3 subunit of AMPA receptors. *Hear Res* 344: 284-294

Gécz J, Barnett S, Liu J, Hollway G, Donnelly A, Eyre H, Eshkevari HS, Baltazar R, Grunn A, Nagaraja R *et al* (1999) Characterization of the Human Glutamate Receptor Subunit 3 Gene (GRIA3), a Candidate for Bipolar Disorder and Nonspecific X-Linked Mental Retardation. *Genomics* 62*:* 356-368

Geiger JR, Melcher T, Koh DS, Sakmann B, Seeburg PH, Jonas P, Monyer H (1995) Relative abundance of subunit mRNAs determines gating and Ca2+ permeability of AMPA receptors in principal neurons and interneurons in rat CNS. *Neuron* 15:193–204

Glowatzki E, Fuchs PA (2002) Transmitter release at the hair cell ribbon synapse. *Nature Neuroscience* 5:147–154

Gómez-Nieto R, Rubio ME (2009) A bushy cell network in the rat ventral cochlear nucleus. *The Journal of Comparative Neurology* 516:241–263

Hollmann M, Hartley M, Heinemann S (1991) Ca2+ permeability of KA-AMPA -- gated glutamate receptor channels depends on subunit composition. *Science* 252:851–853

Hu N, Rutherford MA, Green SH (2020) Protection of cochlear synapses from noise-induced excitotoxic trauma by blockade of ca2+-permeable AMPA receptors. *PNAS* 117:3828–3838

Jing Z, Rutherford MA, Takago H, Frank T, Fejtova A, Khimich D, Moser T, Strenzke N (2013) Disruption of the presynaptic cytomatrix protein bassoon degrades ribbon anchorage, multiquantal release, and sound encoding at the hair cell afferent synapse. *The Journal of Neuroscience* 33:4456–4467

Johannesen PT, Lopez-Poveda EA (2021) Age-related central gain compensation for reduced auditory nerve output for people with normal audiograms, with and without tinnitus. *iScience* 24:102658

Khimich D, Nouvian R, Pujol R, tom Dieck S, Egner A, Gundelfinger E D, Moser T (2005) Hair cell synaptic ribbons are essential for synchronous auditory signalling. *Nature* 434:889-894

Kim KX, Payne S, Yang-Hood A, Li SZ, Davis B, Carlquist J, V-Ghaffari B, Gantz JA, Kallogjeri D, Fitzpatrick JAJ *et al* (2019) Vesicular glutamatergic transmission in noise-induced loss and repair of cochlear ribbon synapses. *The Journal of Neuroscience* 39:4434–4447

Kim KX, Rutherford MA (2016) Maturation of NaV and KV Channel Topographies in the Auditory Nerve Spike Initiator before and after Developmental Onset of Hearing Function. *The Journal of Neuroscience* 36:2111-2118

Konrad-Martin D, Dille MF, McMillan G, Griest S, McDermott D, Fausti SA, Austin DF (2012) Age-Related Changes in the Auditory Brainstem Response. *J Am Acad Audiol* 23:018-035

Li N, Carrel L (2008) Escape from X chromosome inactivation is an intrinsic property of the Jarid1c locus. *Proceedings of the National Academy of Science*s 105: 17055-17060

Liberman LD, Wang H, Liberman MC (2011) Opposing Gradients of Ribbon Size and AMPA Receptor Expression Underlie Sensitivity Differences among Cochlear-Nerve/Hair-Cell Synapses. *The Journal of Neuroscience* 31:801-808

Liberman MC (1980) Morphological differences among radial afferent fibers in the cat cochlea: an electron-microscopic study of serial sections. *Hearing Research* 3:45–63

Lozier NR, Muscio S, Pal I, Ming HC, Rubio ME (2023) Sex differences in glutamate AMPA receptor subunits mRNA with fast gating kinetics in the mouse cochlea. *Front Sys Neurosci* 17: 1100505

Luo F, Sclip A, Jiang M, Südhof TC (2020) Neurexins cluster Ca2+ channels within the presynaptic active zone. *The EMBO journal* 39: e103208

Mahadevaiah SK, Royo H, VandeBerg JL, McCarrey JR, Mackay S, Turner JMA (2009) Key features of the X inactivation process are conserved between marsupials and eutherians. *Current biology: CB* 19:1478-1484

Matuz-Mares D, González-Andrade M, Araiza-Villanueva MG, Vilchis-Landeros MM, Vázquez-Meza H (2022) Mitochondrial Calcium: Effects of Its Imbalance in Disease. *Antioxidants* 11:801

McFadden SL, Zheng XY, Ding DL (2000) Conditioning-induced protection from impulse noise in female and male chinchillas. *J. Acoust. Soc. Am* 107:2162–2168

Meyer AC, Frank T, Khimich D, Hoch G, Riedel D, Chapochnikov NM, Yarin YM, Harke B, Hell SW, Egner A et al (2009) Tuning of synapse number, structure and function in the cochlea. *Nature Neuroscience* 12:444-453

Michanski S, Smaluch K, Steyer AM, Chakrabarti R, Setz C, Oestreicher D, Fischer C, Möbius W, Moser T, Vogl C *et al* (2019) Mapping developmental maturation of inner hair cell ribbon synapses in the apical mouse cochlea. *PNAS* 116:6415–6424

Milon B, Mitra S, Song Y, Margulies Z, Casserly R, Drake V, Mong JA, Depireux DA, Hertzano R (2018) The impact of biological sex on the response to noise and otoprotective therapies against acoustic injury in mice. *Biology of sex differences* 9:12

Moverman DJ, Liberman LD, Kraemer S, Corfas G, Liberman MC (2023) Ultrastructure of noise-induced cochlear synaptopathy. *Scientific reports* 13:19456

Müller M, von Hünerbein K, Hoidis S, Smolders JWT (2005) A physiological place-frequency map of the cochlea in the CBA/J mouse. *Hearing Research* 202:63–73

Ohlemiller KK, Gagnon PM (2004) Apical-to-basal gradients in age-related cochlear degeneration and their relationship to " primary " loss of cochlear neurons. *The Journal of Comparative Neurology* 479:103–116

Ohn TL, Rutherford MA, Jing Z, Jung S, Duque-Afonso CJ, Hoch G, Picher MM, Scharinger A, Strenzke N, Moser T (2016) Hair cells use active zones with different voltage dependence of ca2+ influx to decompose sounds into complementary neural codes. *PNAS* 113:E4716–E4725

Payne SA, Joens MS, Chung H, Skigen N, Frank A, Gattani S, Vaughn K, Schwed A, Nester M, Bhattacharyya A *et al* (2021) Maturation of heterogeneity in afferent synapse ultrastructure in the mouse cochlea. *Frontiers in Synaptic Neuroscience* 13:678575

Payne SA, Jones MS, Chung H, Skigen N, Fran A, Gattani S, Vaughn K, Schwed A, Nester M, Bhattacharyya A *et al* (2021) Maturation of heterogeneity in afferent synapse ultrastructure in the mouse cochlea. Front Synaptic Neurosci 13:678575

Puel JL, Pujol R, Tribillac F, Ladrech S, Eybalin M (1994) Excitatory amino acid antagonists protect cochlear auditory neurons from excitotoxicity. *The Journal of comparative neurology* 341:241–256

Puel JL, Ruel J, Gervais d'Aldin C, Pujol R (1998) Excitotoxicity and repair of cochlear synapses after noise-trauma induced hearing loss. *Neuroreport* 9:2109–2114

Purkey A, Dell' Acqua (2020) Phosphorylation-Dependent Regulation of Ca^{2+}-Permeable AMPA Receptors During Hippocampal Synaptic Plasticity. *Front Synaptic Neurosci* 12

Ramirez MA, Ninoyu Y, Miller C, Andrade LR, Edassery S, Bomba-Warczak E, Ortega B, Manor U, Rutherford MA, Friedman RA *et al* (2022) Cochlear ribbon synapse maturation requires nlgn1 and nlgn3. *IScience* 25:104803

Robertson D (1983) Functional significance of dendritic swelling after loud sounds in the guinea pig cochlea. *Hearing Research* 9: 263-278

Rossmann M, Sukumaran M, Penn AC, Veprintsev DB, Babu MM, Greger IH (2011) Subunit-Selective N-terminal domain associations organize the formation of AMPA receptor heteromers. *The EMBO Journal* 30:959–971

Rouse SL, Matthews IR, Li J, Sherr EH, Chan DK (2020) Integrated stress response inhibition provides sex-dependent protection against noise-induced cochlear synaptopathy. Scientific Reports. 10:18063

Rubio ME, Matsui K, Fukazawa Y, Kamasawa N, Harada H, Itakura M, Molnár E, Abe M, Sakimura K, Shigemoto R (2017) The number and distribution of AMPA receptor channels containing fast kinetic glua3 and glua4 subunits at auditory nerve synapses depend on the target cells. *Brain Structure & Function* 222:3375–3393

Ruel J, Bobbin RP, Vidal D, Pujol R, Puel JL (2000) The selective AMPA receptor antagonist GYKI 53784 blocks action potential generation and excitotoxicity in the guinea pig cochlea. *Neuropharmacology* 39:1959–1973

Ruel J, Chen C, Pujol R, Bobbin RP, Puel JL (1999) Ampa-Preferring glutamate receptors in cochlear physiology of adult guinea-pig. *The Journal of Physiology* 518:667–680

Rutherford MA, Moser T (2016) The Ribbon Synapse Between Type I Spiral Ganglion Neurons and Inner Hair Cells. The Primary Auditory Neurons of the Mammalian Cochlea. *Springer Handbook of Auditory Research* 52: 117-156

Rutherford MA, Bhattacharyya A, Xiao M, Cai HM, Pal I, Rubio M E (2023) GluA3 subunits are required for appropriate assembly of AMPAR GluA2 and GluA4 subunits on cochlear afferent synapses and for presynaptic ribbon modiolar-pillar morphology. *eLife* 12: e80950

Sebe JY, Cho S, Sheets L, Rutherford MA, von Gersdorff H, Raible DW (2017) Ca2+-permeable AMPARs mediate glutamatergic transmission and excitotoxic damage at the hair cell ribbon synapse. J Neurosci 37:6162-6175

Shanks NF, Savas JN, Maruo T, Cais O, Hirao A, Oe S, Ghosh A, Noda Y, Greger IH, Yates JR 3rd, *et al* (2012) Differences in AMPA and kainate receptor interactomes facilitate identification of AMPA receptor auxiliary subunit GSG1L. *Cell reports* 1: 590–598

Shuster B, Casserly R, Lipford E, Olszewski R, Milon B, Viechweg S, Davidson K, Enoch J, McMurray M, Rutherford MA *et al* (2021) Estradiol Protects against Noise-Induced Hearing Loss and Modulates Auditory Physiology in Female Mice. *International journal of molecular sciences* 22:12208

Szanto C, Ionescu M (1983) Influence of age and sex on hearing threshold levels in workers exposed to different intensity levels of occupational noise. *Audiol* 22:339–356

Thomas CI, Ryan MA, Kamasawa N, Scholl B (2023) Postsynaptic mitochondria are positioned to support functional diversity of dendritic spines. *eLife* 12:RP89682

Verma M, Lizama BN, Chu CT (2022) Excitotoxicity, calcium and mitochondria: a triad in synaptic neurodegeneration. *Transl Neurodegener* 11:3

Wang YX, Wenthold RJ, Ottersen OP, Petralia RS (1998) Endbulb synapses in the anteroventral cochlear nucleus express a specific subset of AMPA-type glutamate receptor subunits.*The Journal of Neuroscience* 18:1148–1160

Wong AB, Jing Z, Rutherford MA, Frank T, Strenzke N, Moser T (2013) Concurrent maturation of inner hair cell synaptic Ca2+ influx and auditory nerve spontaneous activity around hearing onset in mice. *The Journal of neuroscience: the official journal of the Society for Neuroscience* 33:10661–10666

Wong AB, Rutherford MA, Gabrielaitis M, Pangrsic T, Göttfert F, Frank T, Michanski S, Hell S, Wolf F, Wichmann C *et al* (2014) Developmental refinement of hair cell synapses tightens the coupling of Ca2+ influx to exocytosis. *The EMBO Journal* 33:247–264

Zhao H, Lomash S, Chittori S, Glasser C, Mayer ML, Schuck P (2017) Preferential assembly of heteromeric kainate and AMPA receptor amino terminal domains. *eLife* 6:e32056

Figure Legends

Figure 1. ABR wave-I amplitude was reduced, and the threshold was elevated in mice raised in ambient sound.

A) Summary of experimental design: ABRs were recorded at four different time points from the mice raised either in a facility with quiet sound conditions (10 dB SPL; dotted line) or ambient sound (40 dB SPL) solid line). At P35, the GluA3WT and GluA3KO mice (n = 17) were transcardially perfused, and cochleae were collected for further ultrastructural and immunofluorescence, and confocal analyses.

B) ABRs (mean ± SD) show that mice raised in ambient sound levels have similar click thresholds between genotypes ($p = 0.75$; top panel). However, ABR pure tone thresholds were higher in P60 GluA3^{KO} above 16 kHz, while wave-1 amplitude was decreased above 50 dB (pure tones $p < 0.05$, two-way ANOVA; wave-1 amplitude $p < 0.05$, two-way mixed ANOVA) (**top and bottom center; Dataset EV1**). At P90, ABR thresholds were elevated at 32 dB, while click wave-1 amplitude was decreased above 60 dB SPL (clicks $p = 0.07$, pure tones $p < 0.05$; wave-1 amplitude $p < 0.05$) (**top and bottom right; Dataset EV1**) (*$p < 0.05$, **$p < 0.01$, ***$p < 0.001$, ****$p < 0.0001$, two-way mixed ANOVA followed by *post hoc* Holm- Šidák's multiple comparison test). GluA3^{WT} (n = 13; black lines); GluA3^{KO} (n = 14, gray line).

C) ABRs (mean ± SD) of mice raised in quiet show comparable clicks and pure tones thresholds (upper panel) and wave-I amplitude (lower panel) between genotypes at P35. P60 and P90 (two-way mixed ANOVA followed by *post hoc* Holm- Šidák's multiple). GluA3^{WT} (n = 14, black lines), GluA3^{KO} (n = 14, gray lines).

D) Input/output (I/O) slope of ABR wave-I amplitude is significantly declined in GluA3^{KO} mice in ambient at P35 and older ages (left). In contrast, mice in quiet show a similar slope at P35 and older ages between genotypes (right). Analysis of I/O slope from P20 GluA3^{KO} and GluA3^{WT} mice raised in quiet were similar. Each data point shows individual ABR wave-I amplitude (input/output) slope as function of sound intensity. Data represents the median (*$p < 0.05$, **$p < 0.01$, two-way ANOVA followed by *post hoc* Tukey multiple comparison test).

Figure 2. Ambient sound triggers ABR click wave-I amplitude reduction in female GluA3^{KO} mice.

A) GluA3^{WT} mice raised in ambient and quiet (mean ± SD) show similar ABR click and pure tones thresholds (upper panel), and click wave-I amplitude (lower panel) at P35, P60 and P90 (two-way mixed ANOVA followed by *post hoc* Holm-Šidák's multiple). Data represented as mean ± SD.

B) ABR click and pure tones thresholds (upper panel), and click wave-I amplitude analysis (lower panel) from P35, P60, and P90 GluA3^{KO} mice raised in ambient and in quiet. Wave-I amplitude was significantly reduced in GluA3^{KO} raised in ambient compared to GluA3^{KO} mice raised in quiet (*$p < 0.05$, **$p < 0.01$, ***$p < 0.001$, ****$p < 0.0001$, two-way mixed ANOVA followed by *post hoc* Holm- Šidák's multiple). Data represented as mean ± SD.

Figure 3. Synapse counts for 5-week old females raised in ambient sound or in quiet. Number per inner hair cell for all synapses and divided into 3 tonotopic regions centered at 10, 20, or 40 kHz; GluA3^{WT} (black), GluA3^{KO} (gray); Ambient (left, filled circles, n = 20 WT and 61 KO images), Quiet (right, open circles, n = 15 WT and 26 KO images). Markers are image means and bars are means of group means. Two-tailed Mann-Whitney U test with Holm- Šidák's correction for multiple comparisons; ns $p > 0.05$, * $p < 0.05$, ** $p < 0.01$, *** $p < 0.001$.

A) Paired synapses (CtBP2 + GluA2 + GluA4) were not significantly different in number between GluA3^{WT} and GluA3^{KO} for all synapses or in any of the 3 tonotopic regions in ambient sound or in quiet.

B) Lone ribbons (CtBP2 only) were significantly greater in number in GluA3^{KO} than GluA3^{WT} in ambient sound; not significantly different in quiet.

C) Ribbonless synapses (GluA2 + GluA4) were significantly greater in number in GluA3^{KO} than GluA3^{WT} in ambient sound; but significantly fewer in quiet.

D) Synapses lacking detectable GluA4 (CtBP2 + GluA2 only) were significantly fewer in number in GluA3^{KO} than GluA3^{WT} in ambient sound; not significantly different in quiet.

E) Synapses lacking detectable GluA2 (CtBP2 + GluA4 only) were sometimes observed, only in GluA3^{KO}, but not significantly different in number in ambient sound or in quiet.

Figure 4. AMPAR intensity analysis of synapses from 5-week-old females raised in ambient sound or quiet. GluA3^{WT} (black), GluA3^{KO} (gray); Ambient (left, filled circles, n = 7 WT and 7 KO images), Quiet (right, open circles, n = 7 WT and 7 KO images). Markers are image means and bars are means of group means. Two-tailed Mann-Whitney U test with Holm- Šidák's correction for multiple comparisons; ns $p > 0.05$, * $p < 0.05$, ** $p < 0.01$, *** $p < 0.001$. Image means were normalized to the WT group mean per sound condition in panels A – C.

A) For GluA4 intensity per synapse, there was no significant difference between genotypes in ambient or in quiet conditions.

B) For GluA2 intensity per synapse, there was no significant difference between genotypes in ambient, but GluA3^{WT} synapses had more GluA2 fluorescence in quiet conditions.

C) The GluA4:GluA2 intensity ratio per synapse was greater for GluA3^{WT} synapses in both ambient and in quiet conditions.

D) In each image, the mean GluA4:GluA2 intensity ratio for ribbonless synapses was divided by the mean GluA4:GluA2 intensity ratio for paired synapses, such that numbers greater than 1 indicate greater GluA4 fluorescence at ribbonless synapses than paired synapses. Ribbonless

synapses had greater GluA4:GluA2 ratios than paired synapses only for GluA3^{WT} mice in ambient conditions.

Figure 5. AMPA receptor subunit fluorescence ratios in whole synapses and nanodomains from 5-week-old female mice raised in quiet.

A) GluA3^{WT} (upper) and GluA3^{KO} (lower) synapses on inner hair cells in the 38 kHz tonotopic region labeled with anti-CtBP2 (red), anti-GluA4 (blue), and anti-GluA2 (green).

B) Individual synapse with 9 square 13x13 pixel matrices overlaid for nanodomain analysis. Each pixel is 26 nm.

C-D) Frequency histograms of ratios of raw GluA4:GluA2 fluorescence for whole synapses (black, dark red) and nanodomains (gray, light red) for GluA3^{WT} (C) and GluA3^{KO} (D). Data from midcochlea. WT: 1,026 nanodomains in 114 synapses from 4 images; KO: 990 nanodomains in 110 synapses from 4 images.

E) Cumulative histograms of the data in C-D. Comparing genotypes, the distributions of ratios were significantly different for synapses (KS test, $p = 7.2\ e^{-9}$) and for nanodomains within synapses (nanodomains, $p = 3.5\ e^{-19}$).

F) GluA4:GluA2 fluorescence ratios per synapse as a function of ribbon fluorescence. The variables were significantly correlated for GluA3^{WT} but not for GluA3^{KO}. Scale bars: A) 2 μm; B) 100 nm.

Figure 6. Radial distribution of AMPA receptors around synapse center in 5-week-old female mice raised in quiet.

A) Squares were overlaid on synapses in 2-dimensional maximum-intensity projections to create shells for calculation of 1-dimensional radial distributions of blue to green fluorescence density to approximate changes in the relative abundance of GluA4:GluA2 as a function of distance from ribbon center.

B) Examples of synapses from $GluA3^{WT}$ (upper) and $GluA3^{KO}$ (lower).

C) Upper left: Radial distribution of raw shell densities for the WT synapse in (A) for CtBP2 (red), GluA4 (blue), and GluA2 (green). In black is the ratio of raw blue to green fluorescence. Upper right: Ratio of raw GluA4:GluA2 shell densities for the WT synapses from the image of the 11 kHz region; single synapse on the left is shown in thick black trace; the image mean is shown in the dashed red trace. Lower left: Radial distribution for the same synapse when normalized to the peak shell density of each fluorescence channel. Lower right: Ratio of peak-normalized GluA4:GluA2 shell densities for the same image.

D) Same as (C) for the KO image from the 11 kHz region.

E) Image means of the ratio of raw shell densities for WT and KO. Group means are in thick dashed lines for WT (black) and KO (red).

F) Same as (E) for the ratio of peak-normalized shell densities

Figure 7. Pre- and post-synaptic ultrastructural features of IHC-ribbon synapses of 5-week-old female GluA3^{WT} and GluA3^{KO} mice.

A-C) Representative transmission electron microscopy (TEM) micrographs of IHC-ribbon synapses of GluA3^{WT} mice raised in ambient sound. Micrographs are from the middle cochlea turn.

A) The micrograph shows a low magnification of one inner hair cell (IHC) in cross-section. Scale bar: 2 μm.

B-C) Micrographs show one modiolar (B) and one pillar (C) side IHC-ribbon synapse. The modiolar-side synapse has two presynaptic ribbons. Scale bar: 0.5 μm. Aff.: afferent.

D-G) Representative TEM micrographs of IHC-ribbon synapses of GluA3^{KO} mice raised ambient sound. Micrographs are from the middle cochlea turn.

D) TEM micrograph showing afferent swellings (asterisks) around IHCs. Scale bar: 5 μm.

E) The micrograph shows a normal-looking double-ribbon modiolar IHC-ribbon synapse, Scale bar: 0.5 μm.

F) Micrograph shows afferent terminal swellings synapsing on an IHC. Scale bar: 2 μm. The inset shows a higher magnification of the white box region. The insets show details of pre- and post-synaptic membranes with the adjacent presynaptic ribbon.

G) Micrograph shows one afferent swelling with a flat postsynaptic membrane but without a pre-synaptic ribbon. Scale bar: 0.5 μm.

H_1-I_3) Representative TEM serial electron micrographs of one IHC-ribbon synapse on the modiolar side (H_1-H_3) and on the pillar side (I_1-I_3) with their corresponding 3D reconstructions (right side) and its 3D reconstruction (right side) of GluA3^{WT} mice raised in quiet. Micrographs are from the middle cochlea turn. Scale bar: 0.5 μm.

J_1-K_3) Representative TEM serial electron micrographs of one IHC-ribbon synapse on the modiolar side (J_1-J_3) and the pillar side (K_1-K_3) with their corresponding 3D reconstructions (right side) of GluA3^{KO} mice raised in quiet. No afferent swellings are observed in the GluA3^{KO} in the quiet. Micrographs are from the middle cochlea turn. Scale bar: 0.5 μm.

Figure 8. Morphometric analysis of mid-cochlear IHC-ribbon synapses of P35 GluA3^{WT} and GluA3^{KO} mice in quiet.

A) Plots of the quantitative data from 3D reconstructions of the PSD and ribbon surface area and volume of GluA3^{WT} (black, upper panel) and GluA3^{KO} mice (gray, lower panel). Data represented as mean ± SD, unpaired t-test, *$p < 0.05$, **$p < 0.01$.

B) Plots of the quantitative data from single ultrathin sections of the PSD length, ribbon major and minor axis, ribbon circularity and roundness, and synaptic vesicles size (SVs) of IHC-ribbon synapses of GluA3^{WT} (black, upper panel) and GluA3^{KO} (gray, lower panel). Data represented as mean ± SD, unpaired t-test, *$p < 0.05$, **$p < 0.01$, Mann-Whitney test.

Figure 9. SV size and pre-synaptic ribbon shape are altered in the 5-week-old GluA3^{KO} female mice in quiet.

A) Violin plots show the quantitative comparison of the surface and volume of PSDs and ribbons obtained from 3D reconstruction between GluA3^{WT} (black) and GluA3^{KO} (gray) mice. One-way ANOVA, *p < 0.05, Data corresponds to median.

B) Violin plots show the quantitative comparison of PSD length, major and minor ribbon, ribbon circularity and roundness, and synaptic vesicle (SV) size per synapse between GluA3^{WT} (black) and GluA3^{KO} (gray). One-way ANOVA, *p < 0.05, **p < 0.01, ***p < 0.001, ****p < 0.0001, Data corresponds to median.

C) Pie charts show the variability in ribbon shape in percentage from round (red) to elongated (purple) as a total (modiolar + pillar), and then separated by modiolar and pillar-side ribbons of GluA3^{WT} (n = 43) and GluA3^{KO} (n = 51). The Major Axis / Minor axis ratio denotes the ribbon shape regardless of the size, as explained in a schematic drawing on the top of the figure.

D) Histograms show the percentage of modiolar and pillar side afferent terminals without and with mitochondria (m (0) and m+, respectively) in the GluA3^{WT} (n=32) and GluA3^{KO} (n=29) mice raised in quiet (left). The histogram on the right shows the percentage of modiolar and pillar side afferent terminals with 1-2 and more than 3 mitochondria per terminal.

Table 1. Data from 3D reconstructions of IHC-ribbon synapses from mice raised in quiet

Genotypes	Parameters	PSD surface area (μm^2)		PSD volume (μm^3)		Ribbon surface area (μm^2)		Ribbon volume (μm^3)	
		M	P	M	P	M	P	M	P
$GluA3^{WT}$	Minimum	0.32	0.30	0.003	0.003	0.05	0.06	0.001	0.002
	25% Percentile	0.36	0.35	0.006	0.003	0.10	0.08	0.003	0.002
	Median	0.46	0.41	0.008	0.005	0.13	0.09	0.003	0.004
	75% Percentile	0.63	0.57	0.009	0.010	0.16	0.11	0.004	0.004
	Maximum	0.86	0.90	0.013	0.011	0.25	0.16	0.009	0.006
	Mean	0.51	0.47	0.008	0.006	0.13	0.10	0.004	0.003
	Std. Deviation	0.16	0.17	0.002	0.003	0.04	0.03	0.002	0.001
	Coefficient of variation	32%	37%	30%	50%	34%	26%	54%	36%
$GluA3^{KO}$	Minimum	0.21	0.16	0.002	0.002	0.05	0.05	0.001	0.001
	25% Percentile	0.40	0.31	0.005	0.004	0.09	0.06	0.002	0.002
	Median	0.50	0.51	0.006	0.006	0.10	0.08	0.003	0.002
	75% Percentile	0.74	0.58	0.009	0.007	0.12	0.09	0.004	0.003
	Maximum	0.94	0.71	0.013	0.009	0.16	0.12	0.009	0.004
	Mean	0.55	0.45	0.007	0.006	0.10	0.08	0.003	0.002
	Std. Deviation	0.21	0.17	0.003	0.002	0.03	0.02	0.002	0.001
	Coefficient of variation	38%	38%	40%	40%	27%	25%	53%	31%

M: Modiolar; P: Pillar

Table 2. Data from single ultrathin sections of IHC-ribbon synapses from mice raised in quiet

Genotypes	Parameters	PSD length (nm)		Major axis (nm)		Minor axis (nm)		Circularity		Roundness		SVs size (nm)	
		M	P	M	P	M	P	M	P	M	P	M	P
$GluA3^{WT}$	Minimum	375	474	164	164	1	78	0.26	0.64	0.15	0.34	32	30
	25% Percentile	573	553	198	177	83	134	0.62	0.85	0.34	0.60	37	32
	Median	679	680	226	217	99	146	0.73	0.91	0.43	0.72	38	34
	75% Percentile	756	754	293	244	114	169	0.83	0.92	0.54	0.87	39	35
	Maximum	866	839	387	276	171	219	0.87	0.96	0.59	0.95	42	38
	Mean	663	662	251	215	98	150	0.71	0.87	0.42	0.71	38	34
	Std. Deviation	122	121	68	36	32	33	0.15	0.08	0.12	0.16	2	2
	Coefficient of variation	18%	18%	27%	17%	33%	22%	21%	9%	30%	23%	6%	7%
$GluA3^{KO}$	Minimum	424	305	155	146	68	93	0.55	0.66	0.30	0.37	35	36
	25% Percentile	635	446	198	182	92	105	0.70	0.81	0.40	0.52	38	38
	Median	696	564	216	204	107	131	0.78	0.90	0.46	0.63	40	40
	75% Percentile	743	648	272	232	143	147	0.85	0.94	0.61	0.82	41	41
	Maximum	863	777	405	276	200	201	0.92	0.96	0.82	0.92	43	41
	Mean	678	552	236	207	118	132	0.77	0.87	0.52	0.66	39	40
	Std. Deviation	104	150	61	37	34	31	0.10	0.09	0.15	0.17	2	2
	Coefficient of variation	15%	27%	26%	18%	29%	23%	13%	11%	29%	27%	6%	5%

M: Modiolar; P: Pillar

Fig. 1

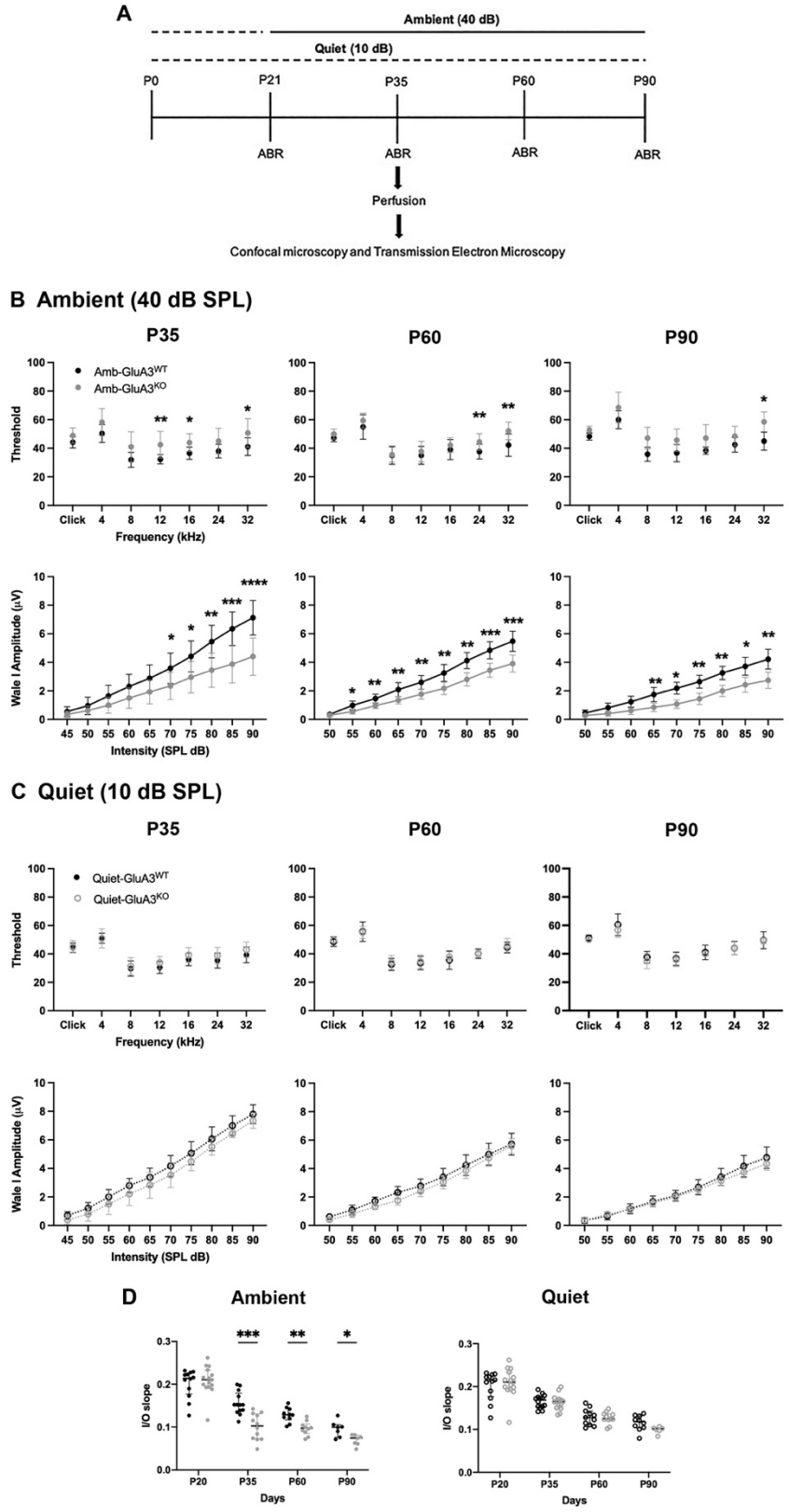
A
Ambient (40 dB)
Quiet (10 dB)
P0
P21
P35
P60
P90
ABR
ABR
ABR
ABR
Perfusion
Confocal microscopy and Transmission Electron Microscopy
B Ambient (40 dB SPL)
P35
P60
P90
Amb-GluA3WT
Amb-GluA3KO
Threshold
Click 4 8 12 16 24 32
Frequency (kHz)
Wale I Amplitude (µV)
45 50 55 60 65 70 75 80 85 90
50 55 60 65 70 75 80 85 90
Intensity (SPL dB)
C Quiet (10 dB SPL)
P35
P60
P90
Quiet-GluA3WT
Quiet-GluA3KO
Threshold
Click 4 8 12 16 24 32
Frequency (kHz)
Wale I Amplitude (µV)
Intensity (SPL dB)
D
Ambient
Quiet
I/O slope
P20 P35 P60 P90
Days

Fig. 2

A GluA3^{WT} Ambient vs Quiet

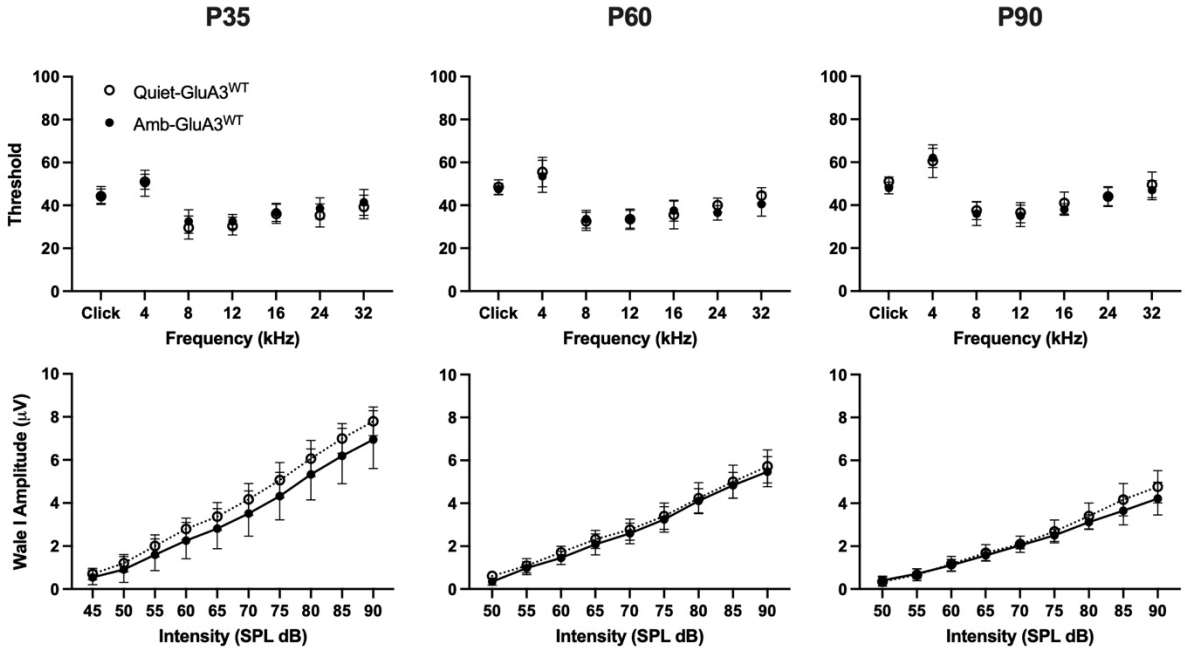

B GluA3^{KO} Ambient vs Quiet

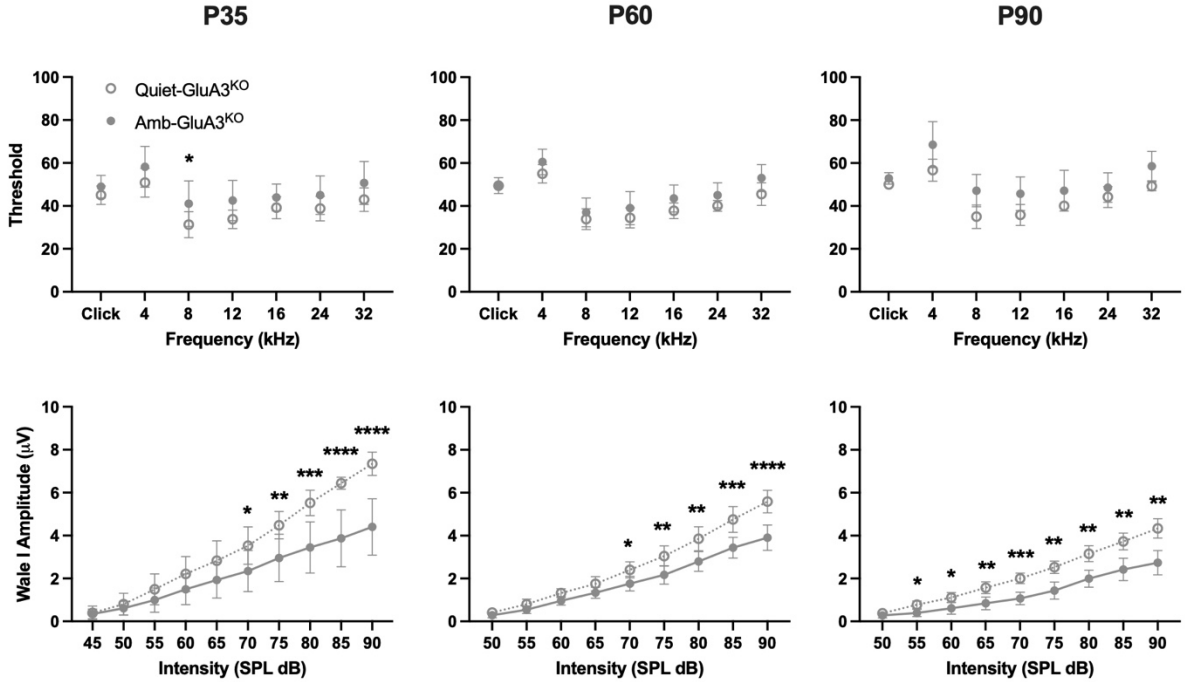

Fig. 3

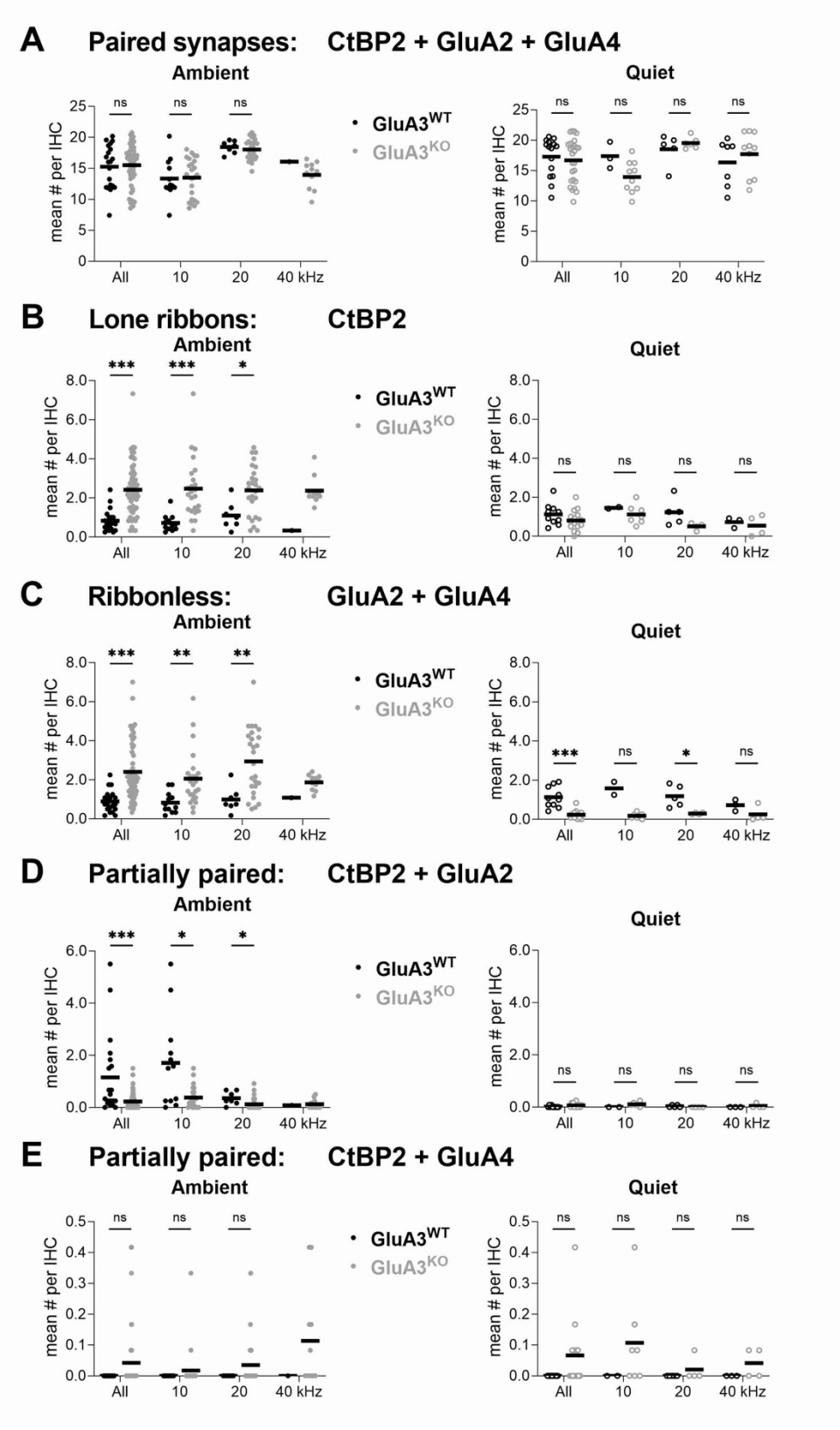
A
Paired synapses: CtBP2 + GluA2 + GluA4
Ambient
Quiet
mean # per IHC
ns
All
10
20
40 kHz
GluA3WT
GluA3KO
B
Lone ribbons: CtBP2
Ambient
Quiet
***
*
C
Ribbonless: GluA2 + GluA4
Ambient
Quiet
**
D
Partially paired: CtBP2 + GluA2
Ambient
Quiet
E
Partially paired: CtBP2 + GluA4
Ambient
Quiet

Fig. 4

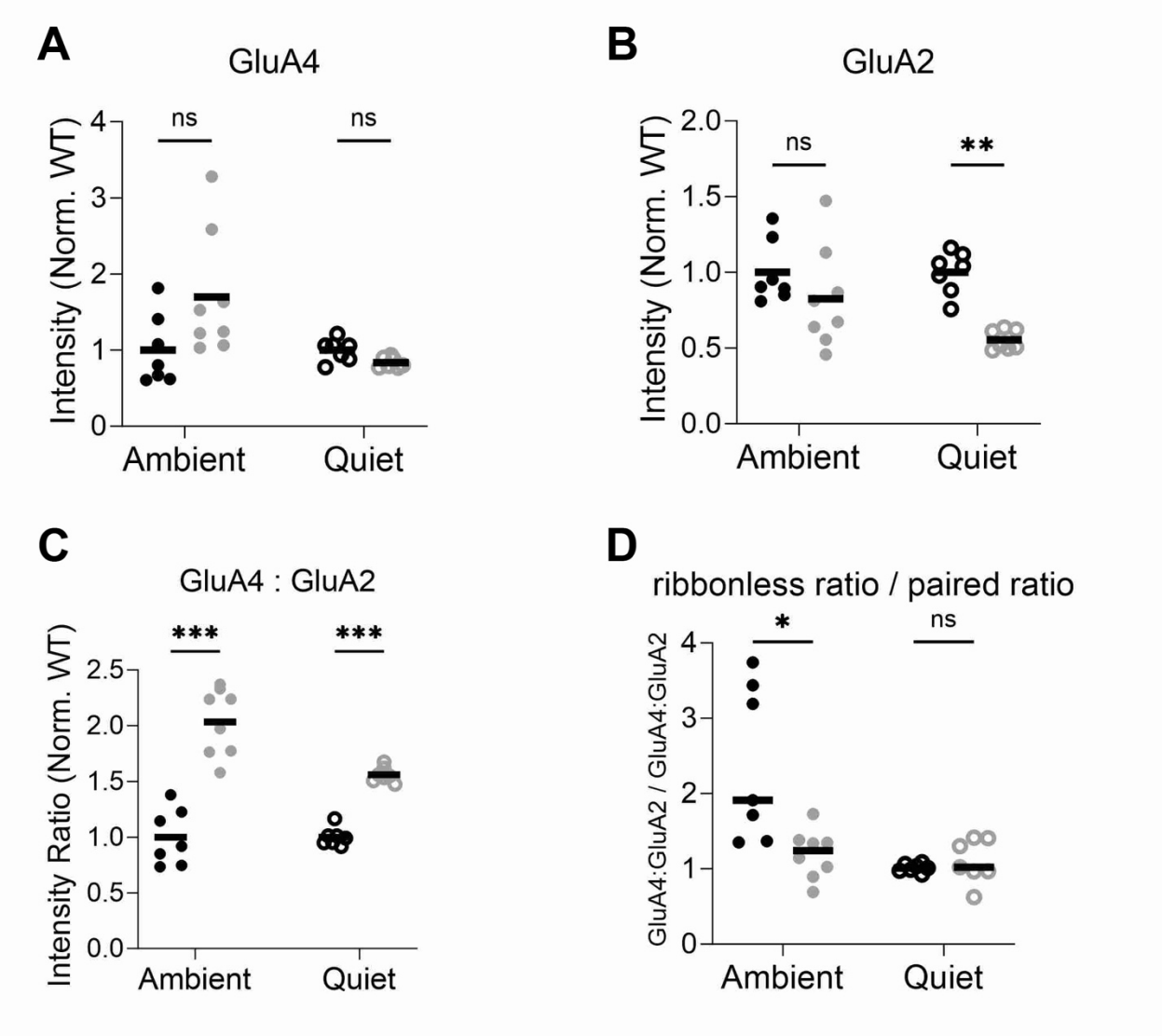
A
GluA4
Intensity (Norm. WT)
ns
ns
Ambient
Quiet
B
GluA2
Intensity (Norm. WT)
ns
**
Ambient
Quiet
C
GluA4 : GluA2
Intensity Ratio (Norm. WT)
***
***
Ambient
Quiet
D
ribbonless ratio / paired ratio
GluA4:GluA2 / GluA4:GluA2
*
ns
Ambient
Quiet

Fig. 5

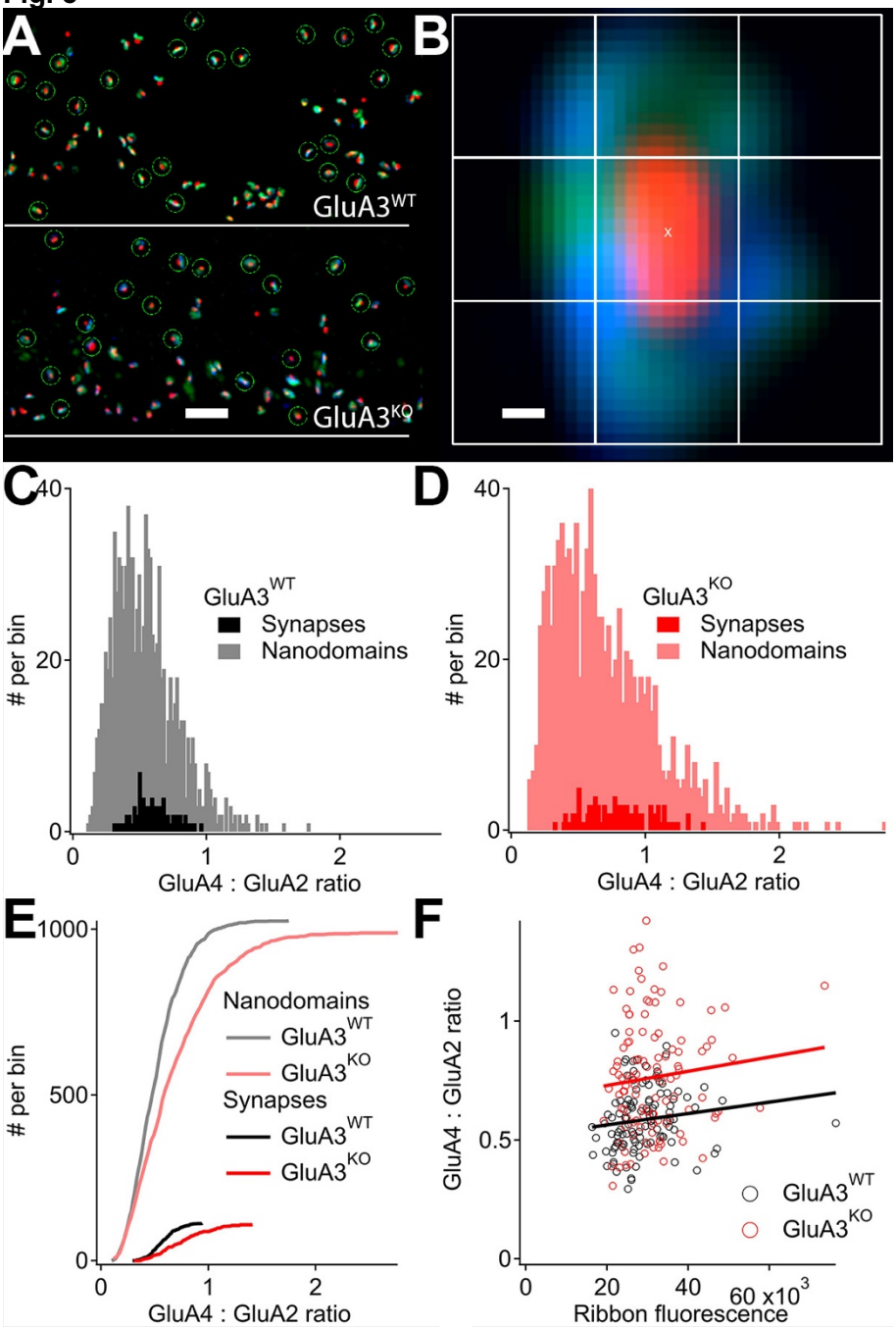
A
GluA3WT
GluA3KO
B
C
per bin
GluA3WT
Synapses
Nanodomains
GluA4 : GluA2 ratio
D
GluA3KO
Synapses
Nanodomains
GluA4 : GluA2 ratio
E
per bin
Nanodomains
GluA3WT
GluA3KO
Synapses
GluA3WT
GluA3KO
GluA4 : GluA2 ratio
F
GluA4 : GluA2 ratio
GluA3WT
GluA3KO
Ribbon fluorescence
60 x10^3

Fig. 6

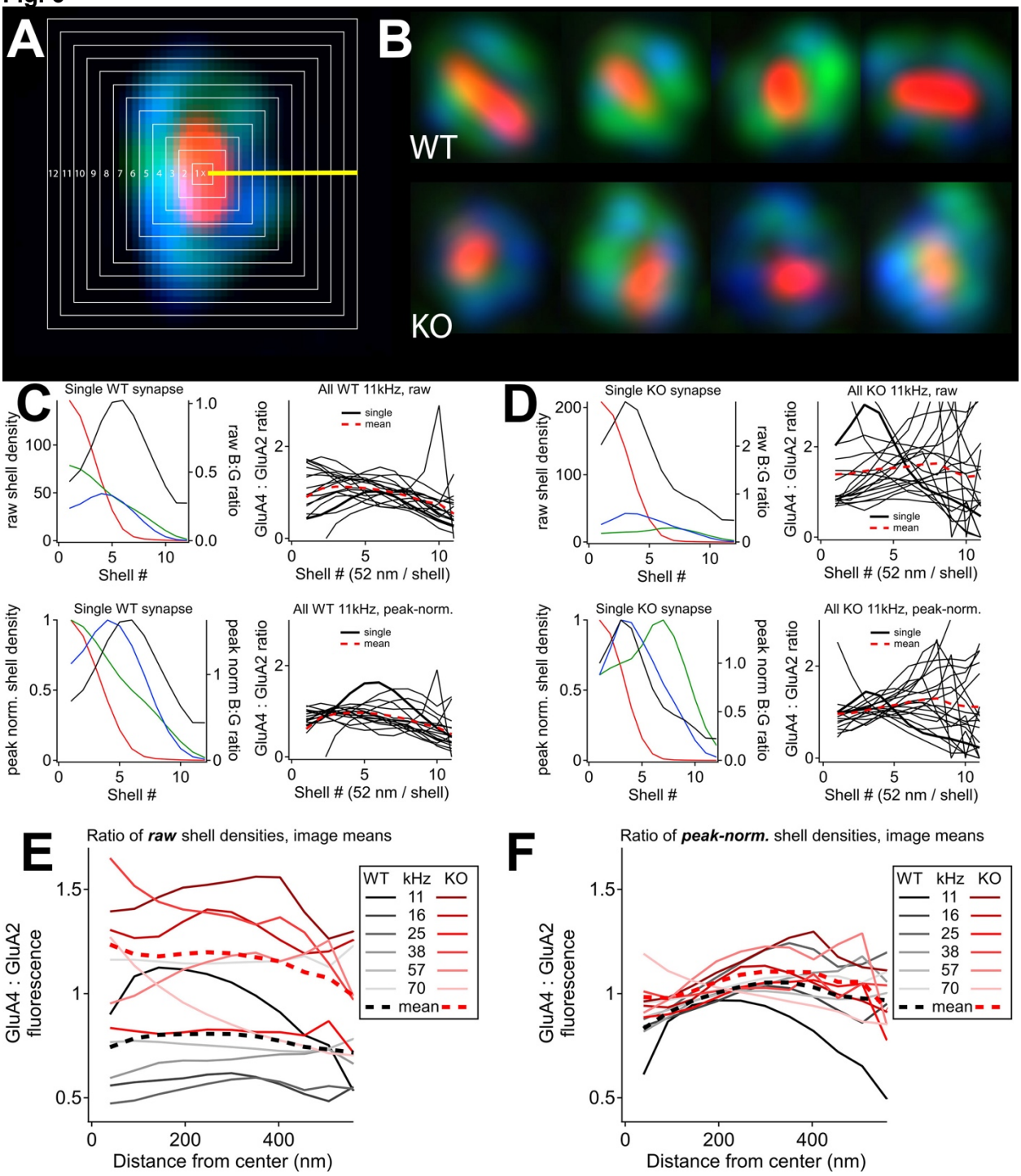
A
B
WT
KO
C
Single WT synapse
raw shell density
raw B:G ratio
Shell #
All WT 11kHz, raw
GluA4 : GluA2 ratio
Shell # (52 nm / shell)
single
mean
D
Single KO synapse
All KO 11kHz, raw
Single WT synapse
peak norm. shell density
peak norm B:G ratio
All WT 11kHz, peak-norm.
Single KO synapse
All KO 11kHz, peak-norm.
E
Ratio of raw shell densities, image means
GluA4 : GluA2 fluorescence
Distance from center (nm)
WT kHz KO
11
16
25
38
57
70
mean
F
Ratio of peak-norm. shell densities, image means

Fig. 7

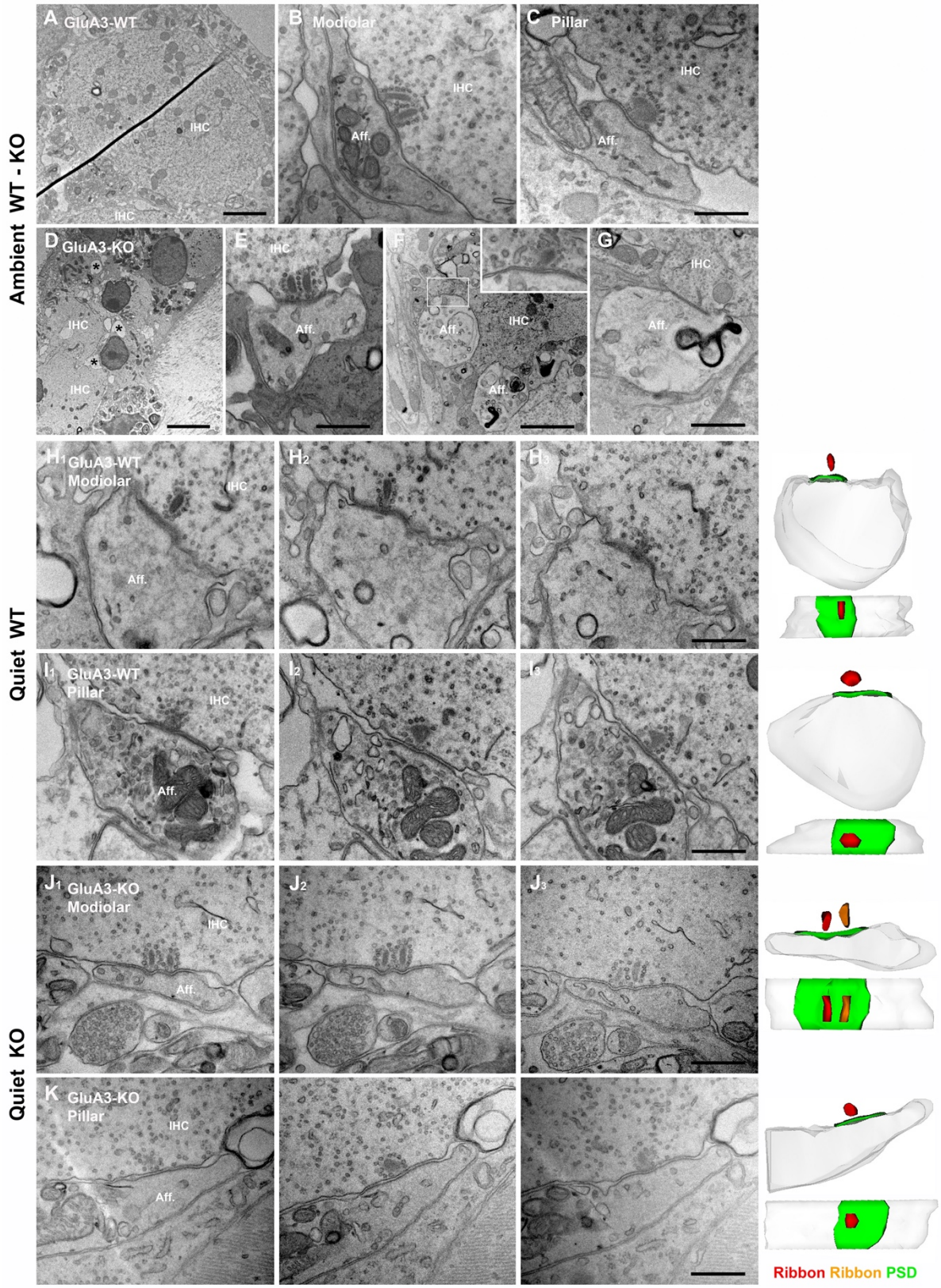
Ambient WT - KO
A GluA3-WT
IHC
IHC
B Modiolar
IHC
Aff.
C Pillar
IHC
Aff.
D GluA3-KO
IHC
IHC
E
IHC
Aff.
F
Aff.
IHC
Aff.
G
IHC
Aff.
Quiet WT
H1 GluA3-WT
Modiolar
IHC
Aff.
H2
H3
Quiet KO
I1 GluA3-WT
Pillar
IHC
Aff.
I2
I3
J1 GluA3-KO
Modiolar
IHC
Aff.
J2
J3
K GluA3-KO
Pillar
IHC
Aff.
Ribbon Ribbon PSD

Fig. 8

A Data from 3D reconstructions

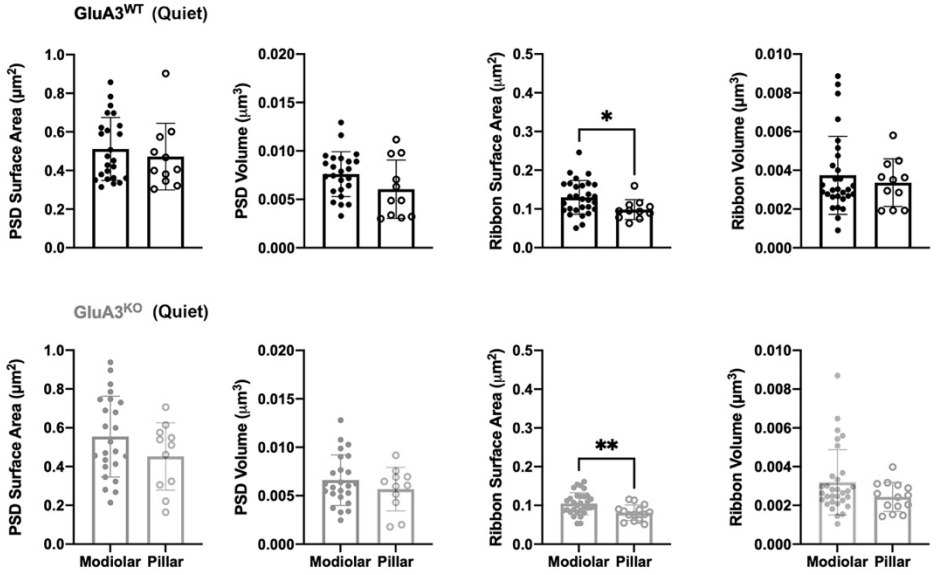

B Data from single ultrathin sections

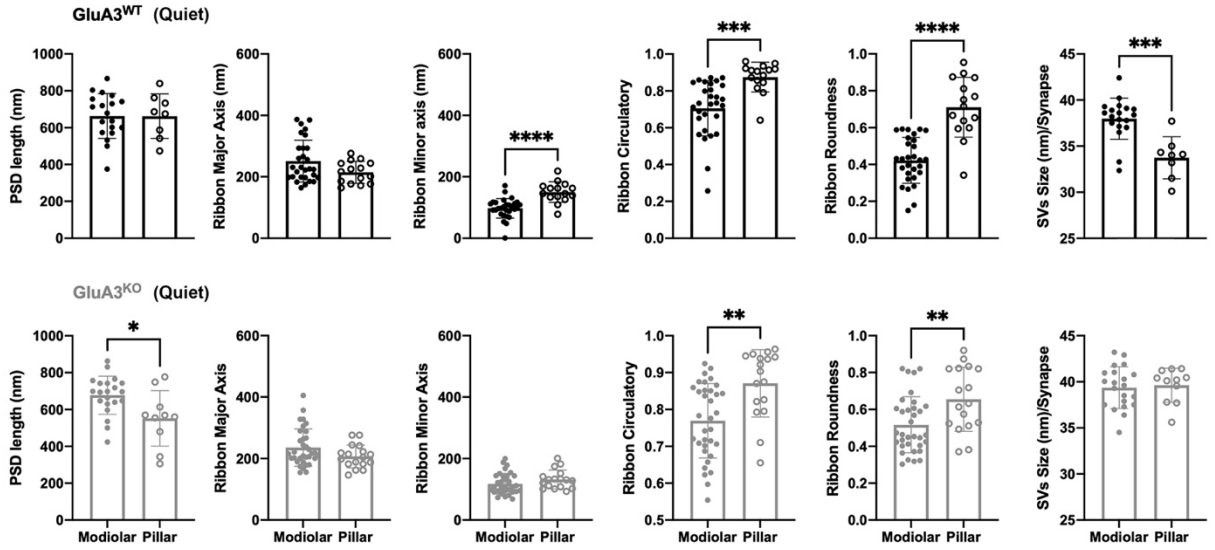

Fig. 9

A Data from 3D reconstructions

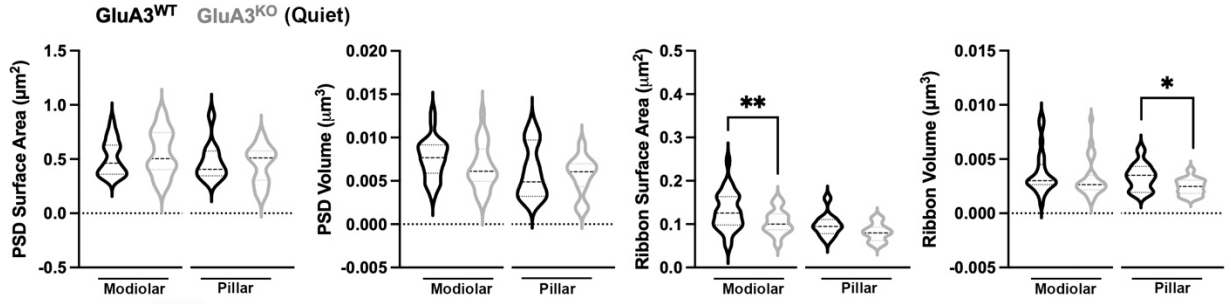

B Data from single ultrathin sections

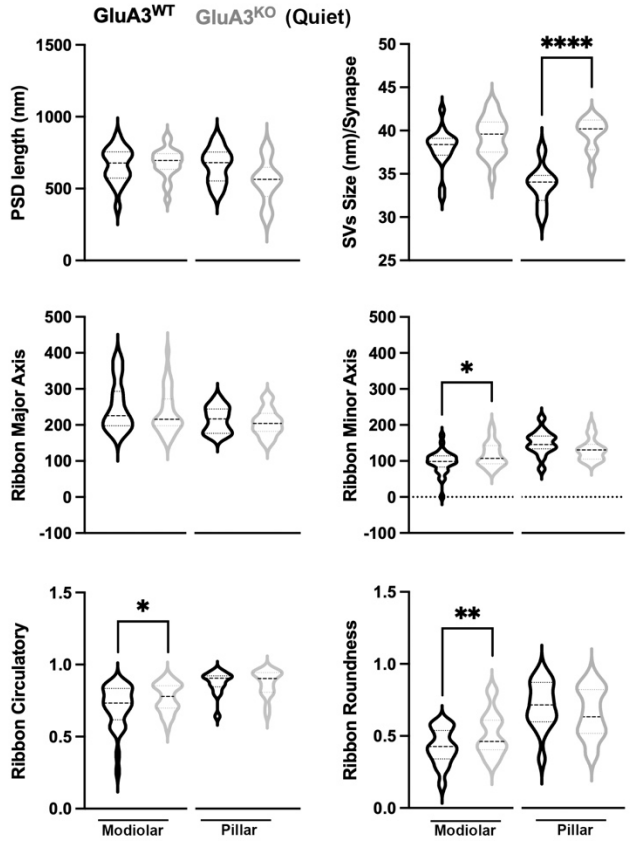

C

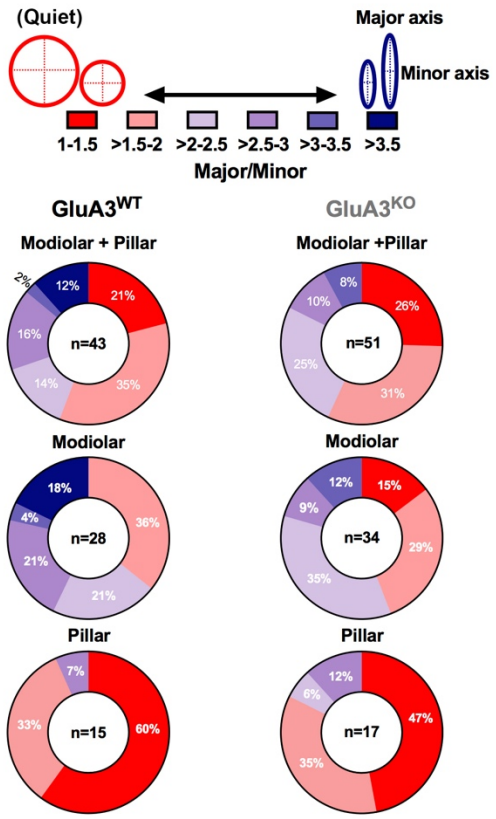
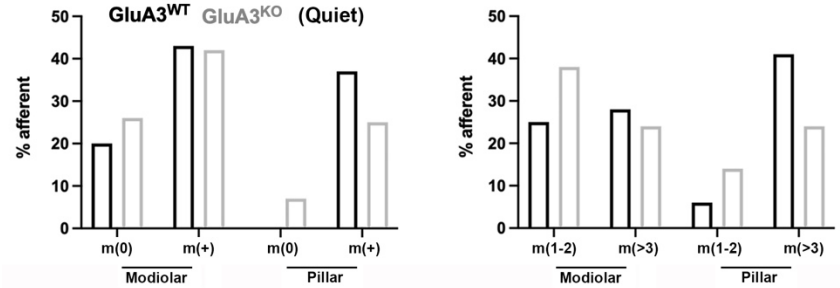
D Afferent terminals with or without mitochondria